Title
Improving the Mechanical Strength and Power Conversion Efficiency of High Temperature Thermoelectrics

Author
Ma, James Minh

Publication Date
2014

Peer reviewed|Thesis/dissertation

UNIVERSITY OF CALIFORNIA

Los Angeles

Improving the Mechanical Strength and Power Conversion Efficiency of High Temperature Thermoelectrics

A dissertation submitted in partial satisfaction of the

requirements for the degree Doctor of Philosophy

in Materials Science and Engineering

By

James Minh Ma

2014

ABSTRACT OF THE DISSERTATION

Improving the Mechanical Strength and Power Conversion
Efficiency of High Temperature Thermoelectrics

by

James Minh Ma

Doctor of Philosophy in Materials Science and Engineering

University of California, Los Angeles, 2014

Professor Richard B. Kaner, Chair

Thermoelectrics are solid state energy conversion materials which are able to generate power through the Seebeck effect or provide cooling through the Peltier effect. Thermoelectric generators have consistently demonstrated their extraordinary reliability and longevity in support of the National Aeronautics Space Administration's (NASA) deep space science and exploration missions. The state-of–practice "heritage" TE materials exhibit only modest thermal-to-electric energy conversion performance, resulting in relatively low system-level conversion efficiencies of 6 to 6.5%.

New thermoelectric devices are sought with improved efficiency to enhance mission capabilities and reduce cost. The refractory material lanthanum telluride ($La_{3-x}Te_4$) is a promising material which is stable up to 1000 ^{o}C and has been shown to have an improved thermoelectric efficiency compared to legacy materials at the same temperature. However, a challenge in the translation of $La_{3-x}Te_4$ as a material into a functional thermoelectric device is

that it is mechanically weak and brittle. A mechanically robust thermoelectric material is desirable to simplify handling during manufacturing, improve device yield, and to increase tolerance to the thermomechanical stresses encountered during operation.

The initial emphasis this work is the characterization of the mechanical properties of the $La_{3-x}Te_4$. The Vicker's hardness and indentation fracture toughness are employed as a rapid, nondestructive technique to evaluate the material. It provides a measure of hardness, a property strongly interlinked with other mechanical properties and important to the resistance to surface flaw formation. In addition, measurement of the cracks formed during hardness testing provides a measure of brittleness of the material in the form of indentation fracture toughness. The strength of the material is measured through flexural testing. The test is destructive and in additional to flexural strength, provides insight into the dominant failure modes of the material. Identification of the failure modes is important to developing mitigation schemes to improve the mechanical performance of the material.

In addition to mechanical performance, enhancements to the thermoelectric performance of lanthanum telluride are also explored through two means. First, the development of lanthanum telluride composites utilizes the concept of the ideal thermoelectric which would combine the favorable properties of different material types. A 50% improvement in efficiency was achieved for composite of $La_{3-x}Te_4$ with a percolated nickel network. The nickel lowered the electrical resistivity of the material while favorably maintaining other thermoelectric transport properties. Second, alkali earth doping with calcium was explored as a means to modify the band structure of the material to improve the Seebeck coefficient. Although calcium doping did not change performance significantly, it provided important lessons into how to modify the band structure of the material to improve the Seebeck coefficient.

The dissertation of James Minh Ma is approved.

Bruce S. Dunn

Jenn-Ming Yang

Delroy A. Baugh

Richard B. Kaner, Committee Chair

University of California, Los Angeles

2014

This work is dedicated to the family, and friends, and especially Sara.

Table of Contents

L**ist of Figures**

Acknowledgements

I am very grateful to everyone I have interacted with over the years and the knowledge, skills, and wisdom they have imparted onto me. First, I am thankful to my adviser Professor Richard Kaner for giving me the opportunity to complete my degree and for all of the support and encouragement over the years. Also, I am very thankful to adviser at JPL, Dr. Jean-Pierre Fleurial. It's been inspiring to work with someone with such expertise, skill, and intuition. I have become a much better scientist because of his high expectations and willingness to pursue new ideas.

Special thanks Dr. Sabah K. Bux for being a mentor and a friend. She spent many hours in the teaching me everything I needed to know to get started in my research. She has also been very supportive and helpful in navigating the sometimes complicated path of our work.

George Nakatsukasa has taught me a lot of what I know about keeping machines working so I could collect data and graduate. He has also been instrumental in teaching me to simplify complex ideas and develop straightforward solutions.

I am grateful to Dr. Frank Kyte for his many hours of help with the electron microprobe and Dr. Sergey Prikhodko for his help with transmission electron microscopy. It also has been a great experience working with Dr. Paul Von Allmen and Dr. Trinh Vo with their expertise on computational modeling. Their work and discussions with them have been very useful helping make sense of experimental data.

Thank you to Samantha M. Clarke for being an excellent undergraduate student. I hope you learned as much from me as I learned from you. Also thank you to Diana Yu for your help as an undergraduate researcher.

I am also thankful for to the fellow students working at JPL Dr. Kurt Star and Danny King for their technical help and lively discussions in the office. Also thanks to Lance Brockway for all of your help proofing articles and my thesis. I would also like to thank to the other members of the Kaner group: especially Chris Turner for all of his help designing and repairing equipment, Dr. Reza Mohammadi for his support, guidance, and constant reminder to focus and finish, and Jaime Torres for suffering with me during those long trips to and from UCLA. Also thank you to all my friends and family for being so supportive over these years.

VITA

2007 B.S., Chemical Engineering, University of California San Diego, La Jolla, California

2008 M.S., Chemistry, University of California San Diego, La Jolla, California

2009 M.S., Materials Science and Engineering, University of California Los Angeles, Los Angeles, California

PUBLICATIONS

Samantha M. Clarke*, James M. Ma*, C.-K. Huang, Paul A. von Allmen, Trinh Vo, Richard B. Kaner, Sabah K. Bux and Jean-Pierre Fleurial (2013). Optimizing Thermoelectric Efficiency of $La_{3-x}Te_4$ with Calcium Metal Substitution. MRS Proceedings, 1490, pp 83-88. doi:10.1557/opl.2013.25. (* These authors contributed equally to this paper)

James M. Ma, Samad A. Firdosy, Richard B. Kaner, Jean-Pierre Fleurial, Vilupanur A. Ravi (2014). Hardness and Fracture Toughness of Thermoelectric $La_{3-x}Te_4$. Journal of Materials Science **49**, 3, 1150-1156.

PUBLICATIONS IN PREPARATION

James M. Ma, Samad A. Firdosy, Jean-Pierre Fleurial, Richard B. Kaner, and Vilupanur A. Ravi. "Equibiaxial Flexural Strength and Weibull Analysis of the Thermoelectric $La_{3-x}Te_{4.}$" (2014)

James M. Ma, Paul von Allmen, Sergey Prikhodko, Trinh Vo, Richard B. Kaner, Sabah K. Bux, Jean-Pierre Fleurial. "Enhanced zT in $La_{3-x}Te_4$-Ni Composites" (2014)

Chapter 1: Introduction to Thermoelectric Materials

1.1 Thermoelectric Operation Principles

Thermoelectrics are materials that can be used for solid state energy conversion and which can serve as a direct link between thermal and electrical energy. Thermoelectric devices can function in two modes: First, a voltage is generated when a temperature difference is induced across a material through the Seebeck effect. Conversely, creating a potential difference across a material generates a thermal gradient that can be used in applications such as heating and cooling through the Peltier effect.

In a typical device, both a p-type and a n-type doped segment are needed to create a thermoelectric couple as shown in Fig. 1. The couple is connected thermally in parallel and electrically in series. In the power-generating configuration, heat from the hot side of the material drives majority carriers towards the cold side so that current flows in one direction. In the cooling/heating configuration, the carriers move in response to the electric field transferring heat from one side to the opposite side.

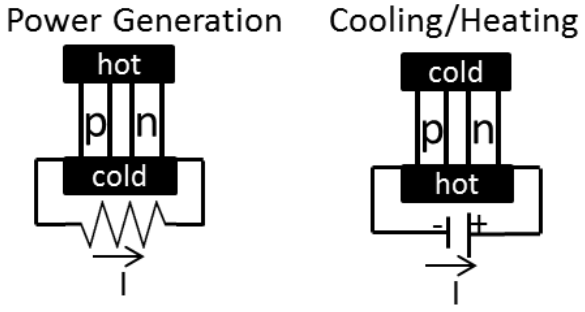

Fig. 1.1 A thermoelectric couple with a p-type and n-type segment can be used for either power generation or heating and cooling. Each segment is linked thermally in parallel and electrically in series.

For power-generation, a thermal gradient is applied to one side of the material driving majority carriers away from the hot side to the cold side which creates a voltage. In the cooling/heating configuration, an electric field drives majority carriers creating a thermal gradient.

The performance of a thermoelectric device is a function of the dimensionless figure of merit ZT, the hot side temperature of the material, and Carnot efficiency. The power conversion efficiency for a given device can be expressed as:

$$\eta = \frac{T_H - T_C}{T_H} \frac{\sqrt{1+ZT}-1}{\sqrt{1+ZT}+\frac{T_C}{T_H}} \tag{1}$$

while the dimensionless figure of merit ZT is defined as

$$ZT = \frac{S^2}{\rho\kappa} T \tag{2}$$

where S is the Seebeck coefficient, ρ is the electrical resistivity, κ is the thermal conductivity, and T is the temperature. The challenge to increasing ZT is that the parameters that define ZT are coupled and often conflicting. Therefore, it is difficult to increase one parameter within ZT without negatively affecting another[1,2]. For example, the electrical resistivity of a material will decrease as a function of increasing carrier concentration

$$\sigma = \frac{1}{\rho} = ne\mu \tag{3}$$

where σ is the electrical resistivity, ρ is the electrical conductivity, n is the carrier concentration, and μ is the mobility. However, with increasing carrier concentration there is a simultaneous decrease in the Seebeck coefficient and an increase to the electronic contribution to thermal conductivity. The Seebeck coefficient as a function of carrier concentration for metals or

degenerate semiconductors which follow parabolic band and energy scattering behavior can be approximated by the Mott equation[3]:

$$S = \frac{8\pi^2 k_B^2}{3eh^2} m^* T \left(\frac{\pi}{3n} \right)^{2/3} \quad (4)$$

where k_b is the Boltzman's constant, h is Planck's constant, m* is the effective mass of the charge carrier, and n is the carrier concentration. The total thermal conductivity is a sum of the electronic κ_e and lattice thermal conductivity κ_l:

$$\kappa_T = \kappa_e + \kappa_l \quad (5)$$

While κ_l is independent of the carrier concentration and depends strongly upon the crystallographic and band structure of the compound, the κ_e electronic contribution to thermal conductivity is directly related to the electrical conductivity and therefore the carrier concentration through the Wiedemann-Franz law:

$$\kappa_e = L\sigma T = ne\mu LT \quad (6)$$

where L is the Lorenz factor; equal to 2.4 x 10^{-8} $J^2K^{-2}C^{-2}$ for free electrons, but varies depending upon the band structure of each material[1]. Due to conflicting properties the zT for a given material, carrier concentration is typically optimized in the heavily doped semiconductor range of 10^{19}-10^{21} cm^{-3} depending on the specifics of the material[4]. The optimization of these properties can is visualized in Fig. 2.

In addition, these transport properties are a function of temperature, making zT a temperature dependent parameter that needs to be optimized for specific temperature ranges. High temperature materials have the added advantages of an enhanced ΔT and a larger T_H. However, developing low resistance electrical contacts and packaging presents greater

challenges at higher temperatures because of increased thermal stresses and accelerated thermal degradation.

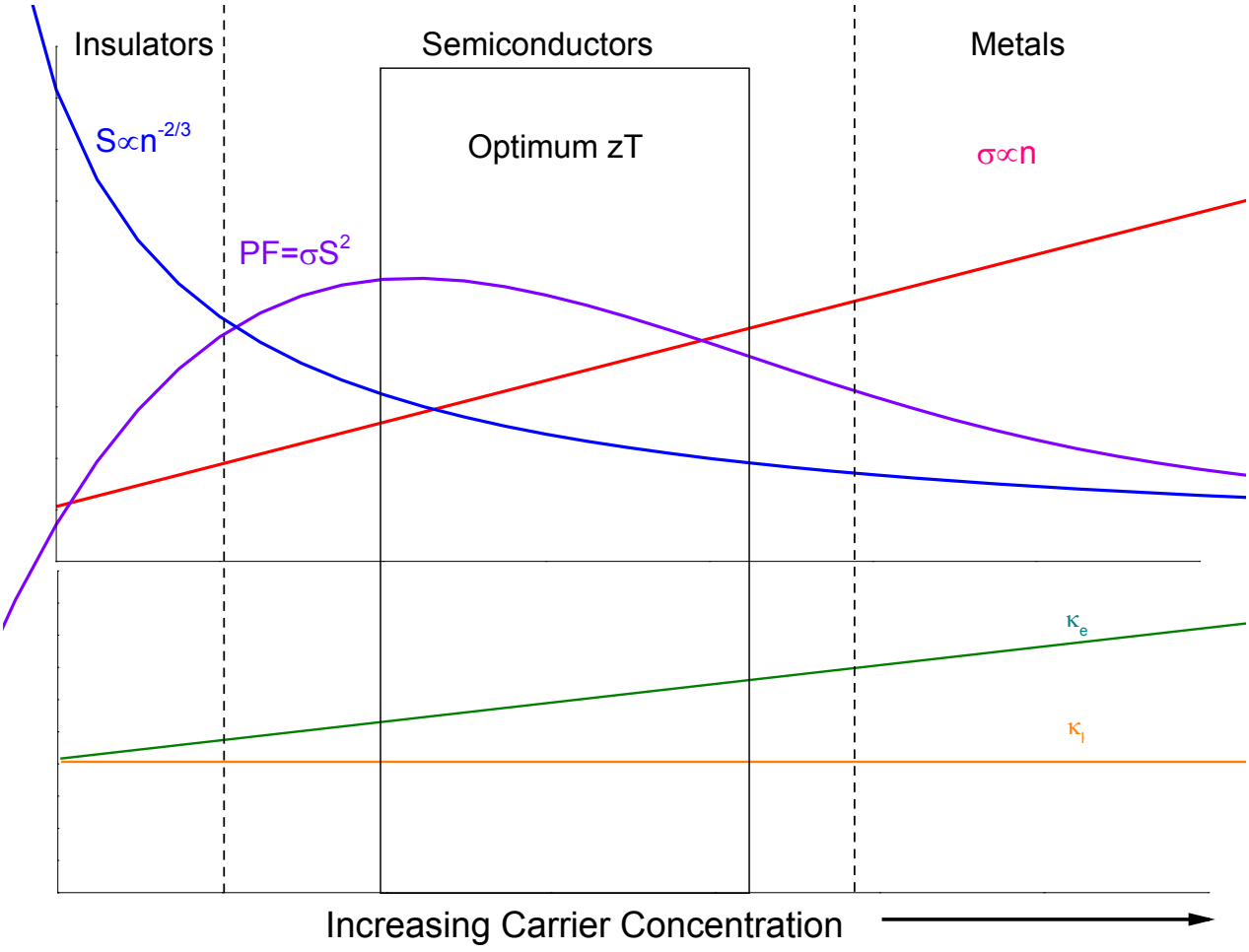

Fig. 1.2 Depiction of transport properties as a function of carrier concentration. The specific region where zT optimizes is material dependent, but is typically in the region of heavily doped semiconductors[4].

1.2 Thermoelectrics in Space

Thermoelectrics have a long and highly successful history of use by NASA for space exploration. There has been a 100% success rate so far in the 18 missions launched by NASA with thermoelectric generators; the most recent being the Mars Science Laboratory named "Curiosity"[5].

These applications have capitalized on the unique advantages of thermoelectrics being an all solid-state means to generate power, where photovoltaics are not suitable (due to lack of solar flux). The lack of moving parts results in high reliability, long lifetimes, and essentially no vibrational noise which can affect instruments. The spacecrafts Voyager 1 and 2 have had 35+ years of continuous use and are currently the furthest human objects in space[6]. There are additional advantages over traditional heat engines which include the use of relatively simple auxiliary systems such as controllers and heat exchangers, the devices have a small form factor, and generators are easily scalable from μW to KW.

1.3 Terrestrial Applications of Thermoelectrics

These advantages have made thermoelectrics attractive for many terrestrial applications. However, the key limitation of thermoelectric materials so far has been their low ZT and hence low efficiencies. This has largely limited their use to niche applications such as remote power systems, space applications, and cooling sensors. The Curiosity rover utilizes a state-of-the-art PbTe based thermoelectric generator that has a 6.5% thermal to electrical conversion efficiency[7].

Currently, pressures to boost energy efficiency and to curb CO_2 output have made thermoelectrics even more attractive. In 2012 it is estimated that the US only used ~40% of its energy contained in fuels towards useful work, with the rest rejected as waste heat[8]. Systems to recover waste heat in automobiles and industrial processes are now being developed[9–13]. For many applications, the use of thermoelectric materials is still prohibitively expensive because of the low device efficiency. Significant gains in ZT are needed before their widespread use becomes feasible. The development of new materials and the careful optimization of their thermoelectric properties continue to be a critical hurdle in the successful widespread implementation of thermoelectric materials in terrestrial applications.

1.4 Advanced Materials for Improved Thermoelectric Efficiency

1.4.1 Introduction to $La_{3-x}Te_4$

Of the rare-earth chalcogenides, $La_{3-x}Te_4$ has been identified as a promising material with a peak ZT of ~1.2 at 1275 K. It possesses the complex Th_3P_4 cubic crystal structure, which is advantageous because the complexity of this structure leads to low thermal conductivity. The unit cell ($Z = 4$) is a defect structure with up to 1/9 of the La atoms missing[14]. The system can be doped by controlling the vacancy content in the structure. $La_{3-x}Te_4$ is solely an n-type conductor and can vary from being an electrical insulator with a charge balanced composition of $La_{2.667}Te_4$ (La_2Te_3) to a stoichiometry of La_3Te_4 which behaves as a metal. The system has been optimized with a vacancy content of $x = 0.23$[15].

Initially made through a melt from the elements, $La_{3-x}Te_4$ was a challenging material to synthesize in reasonable quantities due to an incongruently melting phase diagram and the significant vapor pressure of Te. This made it difficult to achieve the tight stoichiometric control necessary to achieve the optimum carrier concentration. The high temperatures needed during melt synthesis often resulted in appreciable Te loss. As a result, it is difficult to produce large homogeneous ingots with the correct carrier concentration and the maximum ZT. Powder metallurgy was identified as a key method for producing large scale quantities of $La_{3-x}Te_4$ from stoichiometric amounts of the elements[15–17].

1.4.2 Previous Doping of $La_{3-x}Te_4$ with Yb

Computational modeling indicated that the density of states of the valence band is controlled by the La atoms[17]. Substitution for some of the La atoms with a dopant can potentially increase the Seebeck coefficient through modification of the density of states. Currently, $La_{3-x}Te_4$ has a 20% higher ZT when compared to $Si_{0.8}Ge_{0.2}$ and further improvements are sought by modifying the band structure of the system. It was shown that another rare earth, Yb, was able to substitute for La through the same powder metallurgical technique[18]. The carrier concentration of the system can be tuned by adjusting the La^{3+}:Yb^{2+} ratio with Yb^{2+} being the exclusive oxidation state. However, the net effect of doping Yb into the system was only finer carrier concentration control, while a difference in the Seebeck coefficient was not observed.

1.5 Production of Thermoelectric Devices

The production of thermoelectric devices is a complex multistep process. An example simplified process flow diagram for the production of a thermoelectric generator is depicted in Fig. 3. First, the materials are synthesized from the elements or from precursors. The materials are typically synthesized through melt processing or powder metallurgy. Care must be taken to ensure powder homogeneity, proper doping levels, and minimization of contaminants. Newer thin film and nanostructured materials have been developed for research scale production of thermoelectric materials, but currently there are no generators based on these technologies in part due to the low yield and high cost of the deposition techniques[19–24].

Fig. 1.3 High-level process flow diagram for the manufacture of thermoelectric generators.

Next, the material is ground, sieved, and is typically loaded into graphite dies for consolidation of the powders through hot pressing or spark plasma sintering. The material is pressed into high density pellets which serve as the raw materials for the fabrication of thermoelectric legs. Effectiveness of sintering, thermoelectric properties, and mechanical properties can be a function of powder size.

The production of thermoelectric components requires machining of the pressed ingots into thermoelectric legs. A common geometry is a rectangular block with the cross-sectional area

and length optimized based on the electronic and thermal transport properties of the material. The challenge is that many thermoelectric materials are mechanically weak and brittle. Therefore, the components can be a challenge to machine resulting in high failure rates and cost. Cylindrical geometries have been utilized in the past for PbTe based generators in part due the challenge of fabrication. However, the individual sintering of each leg adds to the cost and time of production[25]. After this, the fabricated legs are joined through diffusion bonding, brazing, or some other high temperature stable technique to the hot and cold heat exchangers. Often is it necessary to include metallization layers, diffusion boundary layers, and anti-sublimation coatings to ensure the long term durability of the generator.

There are considerable demands upon thermoelectric materials for successful long term operation. The high operational temperatures (T_{max} ~1273 K) and large temperature differentials (several 100 K) can produce significant stresses upon the material. The transport properties of the materials often result in geometries where ideal thermoelectric elements are narrow (a few mm^2) and several mm long resulting in somewhat delicate parts. Furthermore, the components need to withstand thermal cycling steps necessary for bonding to the heat exchangers and final assembly into the generator. In addition, resistance to thermal cycling and thermal shock will be increasingly important for operational of thermoelectric devices in applications such as waste heat recovery. Therefore, the challenge for thermoelectric materials is not to only produce high zT materials, but the materials must be mechanically sturdy as well.

1.6 Outline of Thesis

The work of this dissertation surrounds the material system $La_{3-x}Te_4$ and can be divided into 3 major areas: 1) characterization of the mechanical properties of $La_{3-x}Te_4$ to provide mechanical design and operational parameters for the implementation of this material in thermoelectric devices; 2) the development of percolated $La_{3-x}Te_4$-Ni composites with enhanced zT; and 3) studying the effects of Ca doping in $La_{3-x}Te_4$ to improve zT. Materials in this temperature range continue to be important for the development of high efficiency radioisotope thermoelectric generators. Furthermore, there exist industrial waste heat sources with temperatures in this range[26]. While research into p-type materials and materials which operate at lower temperatures are also critical, it is beyond the scope of the current work. Instead, the research focuses exclusively on the materials system $La_{3-x}Te_4$ and takes an integrated approach. The aim is to address the key engineering challenge of the relatively poor mechanical properties of this material and as well as fundamental materials research to improve zT.

References

(1) Snyder, G. J.; Toberer, E. S. *Nat Mater* **2008**, *7*, 105–114.

(2) *CRC Handbook of Thermoelectrics*; Rowe, D. M., Ed.; CRC Press, 1995.

(3) Cutler, M.; Leavy, J. F.; Fitzpatrick, R. L. *Phys. Rev.* **1964**, *133*, A1143–A1152.

(4) Bhandari, C.; Rowe, D. *CRC Handb. Thermoelectr.* **1995**.

(5) *Space Radioisotope Power Systems: Multi-Mission Radioisotope Thermoelectric Generator*; 2008.

(6) Yang, J.; Caillat, T. *MRS Bull.* **2006**, *31*, 224–229.

(7) Bechtel, R. *Multi-Mission Radioisotope Thermoelectric Generator*; 2010; Vol. 238.

(8) LLNL-MI-410527. Estimated Energy Use in 2013: ~95.1 Quads, 2013.

(9) Bell, L. E. *Science* **2008**, *321*, 1457–1461.

(10) DiSalvo, F. J. *Science (80-.).* **1999**, *285*, 703–706.

(11) Ball, P.; Caillat, T. *MRS Bull.* **2013**, *38*, 446–447.

(12) Rowe, D. M. *Renew. Energy* **1999**, *16*, 1251–1256.

(13) Meisner, G. P. *Advanced Thermoelectric Materials and Generator Technology for Automotive Waste Heat at GM*; 2011.

(14) Cox, W. L.; Steinfink, H.; Bradley, W. F. *Inorg. Chem.* **1965**, *5*, 318–319.

(15) May, A.; Fleurial, J.; Snyder, G. *Phys. Rev. B* **2008**, *78*, 1–12.

(16) May, A.; Snyder, J.; Fleurial, J. *Sp. Technol. Appl. Int. Forum* **2008**, 672–678.

(17) May, A.; Singh, D.; Snyder, G. *Phys. Rev. B* **2009**, *79*, 1–4.

(18) May, A. F.; Fleurial, J.-P.; Snyder, G. J. *Chem. Mater.* **2010**, *22*, 2995–2999.

(19) Mccormack, J. A.; Fleurial, J. *Mater. Res. Soc. Symp. Proc.* **1991**, *234*, 135–143.

(20) Venkatasubramanian, R.; Colpitts, T.; Watko, E.; Lamvik, M.; ElMasry, N. *J. Cryst. Growth* **1997**, *170*, 817–821.

(21) Yoo, B. Y.; Huang, C. K.; Lim, J. R.; Herman, J.; Ryan, M. A.; Fleurial, J. P.; Myung, N. V. *Electrochim. Acta* **2005**, *50*, 4371–4377.

(22) Boukai, A. I.; Bunimovich, Y.; Tahir-Kheli, J.; Yu, J.-K.; Goddard, W. a; Heath, J. R. *Nature* **2008**, *451*, 168–171.

(23) Tang, J.; Wang, H.-T.; Lee, D. H.; Fardy, M.; Huo, Z.; Russell, T. P.; Yang, P. *Nano Lett.* **2010**, *10*, 4279–4283.

(24) Hochbaum, A. I.; Chen, R.; Delgado, R. D.; Liang, W.; Garnett, E. C.; Najarian, M.; Majumdar, A.; Yang, P. *Nature* **2008**, *451*, 163–168.

(25) Bennett, G. L. In *CRC Handbook of Thermoelectrics*; 1995.

(26) Fleurial, J.-P. *JOM* **2009**, *61*, 79–85.

Chapter 2: Hardness and Fracture Toughness of Thermoelectric $La_{3-x}Te_4$

2.1 The Need for Mechanically Robust High Efficiency Thermoelectric Materials

Thermoelectric generators (TEGs) have a proven record of reliability in space applications with >30 years of continuous service as implemented in the Voyager 1 and 2 missions. Recent advances in materials research have led to higher efficiency materials with roughly a two-fold improvement in energy conversion efficiency over legacy materials such as $Si_{1-x}Ge_x$ and PbTe [1–3]. A significant challenge in developing these new high-efficiency materials into functional devices has been that several of these materials, such as $La_{3-x}Te_4$, behave as weak and brittle ceramics. The fragility of these materials increases the complexity of machining, lowers the yield, and constrains potential device configurations. All of these factors add to the cost and difficulties in developing functional devices.

Efforts are underway to optimize processing conditions and to develop a new class of high-strength high-efficiency materials. However, a baseline understanding of mechanical behavior is necessary for comparisons to be made effectively. Furthermore, fast and reliable means to correlate mechanical behavior to process and composition changes are important to be able to assess progress toward this goal.

Although routinely done for engineering ceramics, the challenges in obtaining mechanical property data for thermoelectric materials are significant because they are weak, brittle, air and water sensitive, and expensive. As a result, for many thermoelectric materials it is difficult to machine specimens into geometries required by standardized testing protocols, such as those prescribed in ASTM standards, for obtaining key properties such as fracture toughness

(K_{IC}) [4,5], flexural strength[6,7], etc. In addition, the stochastic nature of brittle failures requires testing on $n \geq 30$ flexural samples to obtain the Weibull parameters and $n \geq 4$ for fracture toughness from Chevron V-notched beam (CVNB) or single edge notched beam (SENB) testing procedures.

Difficulties in preparing samples of sufficient quality has limited the investigation of fracture toughness to a handful of thermoelectric materials such as Skutterudites, Zn_4Sb_3, and SiGe [8–14]. The challenge of sample preparation is not unique to thermoelectric materials and has been addressed for other brittle ceramic materials with correlation models developed over the past 50+ years which relate K_{IC} to the surface cracks emanating from the corners during Vickers micro-indentation hardness testing [15–24].

Hardness testing stands out as an ideal method to provide information on mechanical properties because it is nondestructive, fast, inexpensive, and requires only limited sample sizes. In addition, the hardness of a material is a complex parameter that is sensitive to the chemical composition, grain size, grain shape, porosity, etc.[25] Although difficult to de-convolute, the hardness value is a measure of many complex phenomena which interact to give rise to mechanical behavior and therefore can be applied as a useful parameter for assessing mechanical behavior.

Empirically determined correlation equations have been developed for many engineering ceramics relating fracture toughness values obtained through procedures outlined by ASTM E 1820 Standard Test Method for Measurement of Fracture Toughness to values calculated from the measurement of crack lengths emanating from the corners of Vickers indentations in brittle materials [16–24,26]. These correlations have proven useful in obtaining good estimates of fracture toughness values in cases where it is difficult to produce acceptable fracture toughness

specimens, a situation relevant to thermoelectric materials [27,28]. In this study, Vickers hardness testing was used to analyze the mechanical characteristics of $La_{3-x}Te_4$. This material is of current significant interest because it has the highest reported efficiency at 1000 ^oC for a bulk n-type material [29]. Hardness and Vickers indentation fracture toughness have been studied as a function of load as a means to evaluate the mechanical behavior of $La_{3-x}Te_4$ and to obtain a measure of fracture toughness.

2.2 Experimental Methods for Hardness and Fracture Toughness Testing

$La_{3-x}Te_4$ was synthesized using powder metallurgical methods first described by May *et al.* [29]. Stoichiometric amounts of the elements with a nominal composition of x = 0.23 were ball milled and followed by hot-pressing to obtain pellets of >98% of theoretical density. The samples were typically 12.7 mm diameter x 1.5 mm thick and are cold mounted in epoxy. The test specimens were polished flat and parallel to ± 0.01 mm. A total of N = 6 samples were metallographically ground and diamond polished using different grit sizes (three samples were finished with 1 μm, two with 0.25 μm, and one with 0.01 μm) to examine if hardness values or fracture toughness were affected by the surface finish. Polishing was accomplished using an oil-based lubricant as $La_{3-x}Te_4$ is water reactive.

Vickers indentation hardness values were measured using an Instron Wilson Hardness Tukon T2100B instrument with a maximum 1 kgf load cell. Best practices as outlined by ASTM C 1327 – 08 Standard Test Method for Vickers Indentation Hardness of Advanced Ceramics were followed for measuring the hardness values of these materials[30]. Optical microscope measurements were carried out under ambient conditions immediately after indentation to

minimize the possibility of environmentally assisted crack growth. A series of N_i = 5 indentations were made for each applied load with a contact time of 10 seconds for N = 6 samples produced under identical processing conditions except for the final surface finish. Grain boundary etching was achieve by soaking a sample polished to a 1 μm diamond finish in a 3 vol % Br_2:MeOH solution for 5 minutes. Samples were examined using a FEI Nova 600 scanning electron microscope (SEM).

2.3 Results and Discussion

2.3.1 Grain Size Determination

Grain size determination was done by using SEM to image a chemically etched surface of highly polished $La_{3-x}Te_4$. A series of 5 images were analyzed using the linear intercept technique and a representative image of the etch surface is shown in Fig. 2.1. The ASTM grain size number determined from the average of the 5 measurements was 16.8 [31]. The grain morphology exhibited a distribution of sizes and each grain appeared regular in shape with no observed elongated grains. There was little visible surface porosity which agrees with the high measured geometric density for these samples.

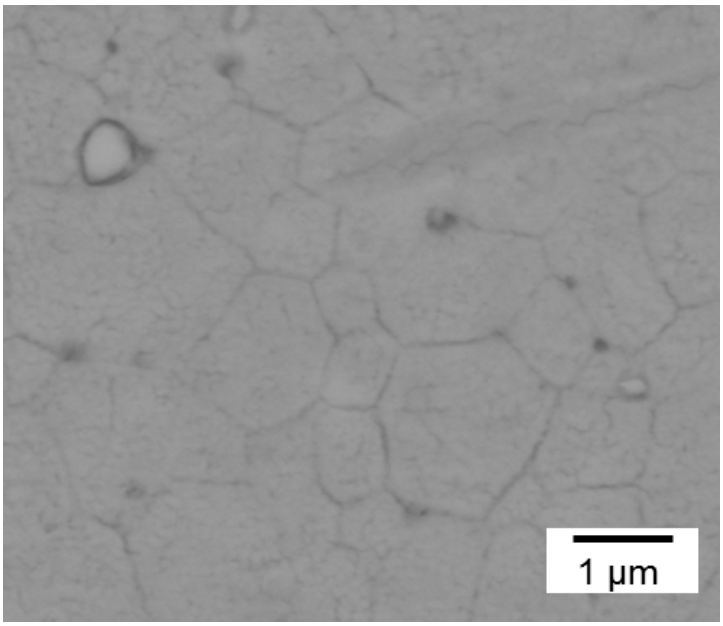

Figure 2.1 Backscattered electron image of a chemically etched $La_{3-x}Te_4$ surface. The ASTM grain size was determined to be 16.8 through the linear intercept technique. Reproduced with permission © (2013) Springer. Journal of Materials Science[32]

2.3.2 Vickers Hardness

The average hardness values of $La_{3-x}Te_4$ are plotted in Fig. 2.2 with error bars of one standard deviation indicated. The average hardness for all samples is represented by the solid line and is the average of 30 indents for each load. The subgroups for samples with surface finishes of 1 µm, 0.25 µm, and 0.01µm are also shown in this figure. The % difference between the mean hardness values (compared between 1 and 0.1 µm surface finish and the 1 and 0.25 µm surface finish samples) were predominantly less than 5%, a number consistent with the reproducibility estimates cited in ASTMC 1327-08[30], thereby justifying taking a global average of hardness values over all the surface finishes used in this study. Therefore, the average of the N

= 6 indents is representative of the hardness of $La_{3-x}Te_4$, i.e, a hardness of HV 439 ± 30 kgf/mm^2 at low loads (0.01kgf) and a hardness of 443 kgf/mm^2 at high loads (0.5 kgf).

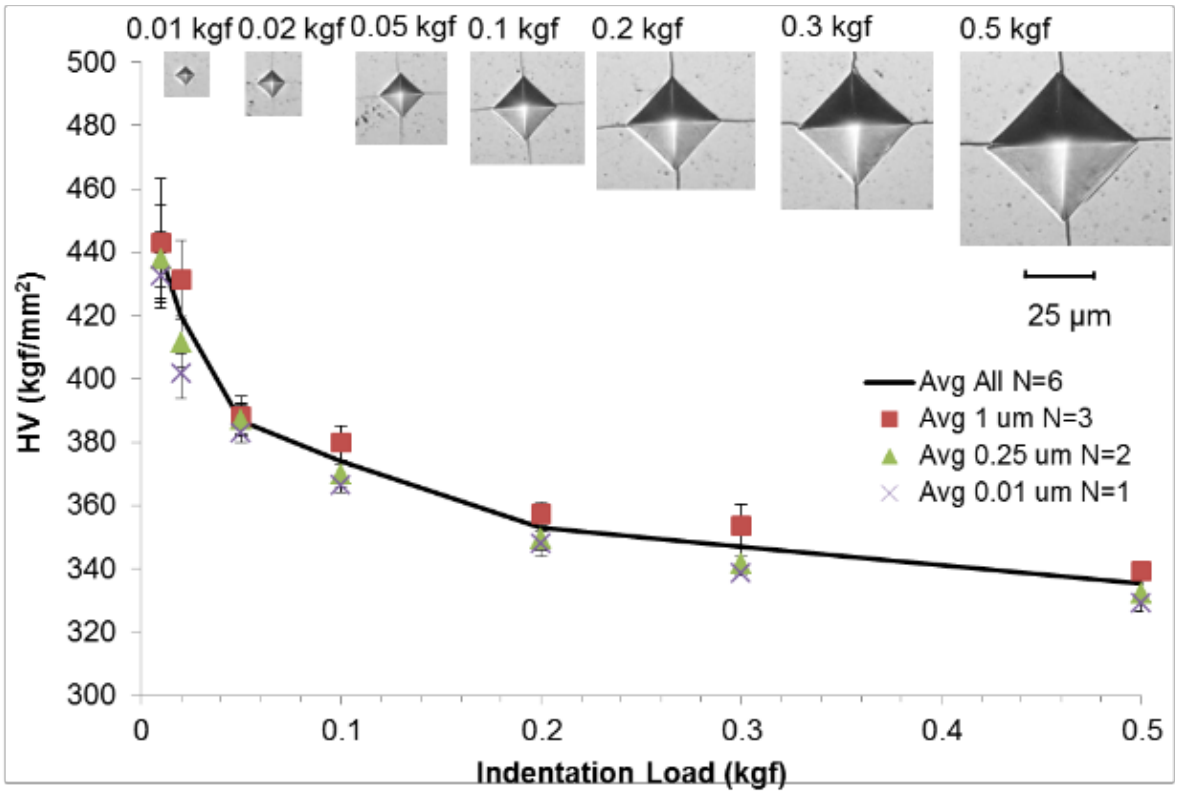

Figure 2.2 Average Vickers hardness values as a function of applied load for $La_{3-x}Te_4$. The solid line represents an average of all surface finishes for N = 6 samples and N_i = 5 indents per sample per applied load. The optical microscope images of samples polished using 0.25 µm diamond paste are provided along the top of the graph (all images are at the same magnification). Spalling occurred above 0.5 kgf so measurements attempted at 1 kgf have been excluded. Error bars represent 1 standard deviation. Reproduced with permission © (2013) Springer. Journal of Materials Science[32]

Optical micrograph images of an indent at each load are shown at the top of the plot. The hardness was measured by determining the position of each corner of the indent to obtain the length of the diagonals for the square indent. The larger error bars at low loads occur as a result of difficulties in accurately measuring the small indentations with an optical microscope. In addition, at low loads there was increased sensitivity due to measurement errors as Vickers Hardness was calculated by the equation:

$$HV = \frac{2F\sin\frac{136^{o}}{2}}{d^{2}} \quad (1)$$

where HV is the Vickers Hardness in kg/mm^2, F is the applied load in kgf, and d is the length of the diagonal in mm. Since d is small for low loads, the error in measurement Δd becomes more significant. Errors in measurement at low loads can be reduced through measurement with a scanning electron microscope, but this was found to be unnecessary given the limited usefulness of the low load data and the added complexity of the measurement [33].

$La_{3-x}Te_4$ is a defect compound with the cubic Th_3P_4 crystal structure [34]. The vacancies in the system control the carrier concentration of the material and the thermoelectric performance [29]. The thermoelectric properties of the material are isotropic and the hardness is expected to be as well because the crystal structure is cubic and the samples are hot pressed randomly dispersed particles. While the hardness may vary as a function of vacancy content, this was beyond the scope of this study. Samples only of thermoelectric interest were studied at the optimized carrier concentration achieved with a vacancy content of x = 0.23

The $La_{3-x}Te_4$ material exhibited crack formation initially at 0.05 kgf and an example of cracking from the Vickers indent is shown in Fig. 2.3. The length of the crack is denoted by l in the image and is measured as a straight line starting from the corner of the indent. As evident in

the micrographs shown in Figs. 2.2 and 2.3, there is pullout and porosity on the surface of the sample which is common for hard and brittle materials. With reduced polishing it is possible to obtain a surface with fewer pullout voids, but with an increased number of scratches. However, as pointed out before, the differences in hardness values between the different surface finishes were small and within acceptable limits of experimental error.

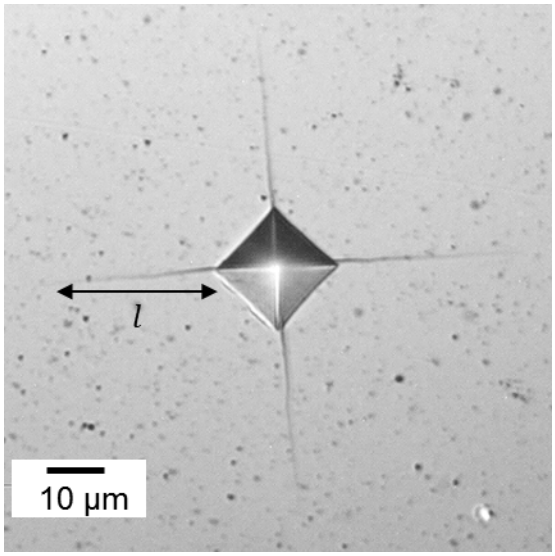

Figure 2.3 Optical micrograph of a Vickers indent on $La_{3-x}Te_4$ with a 0.25 μm surface finish. The indent was made under an applied load of 0.1 kgf. Cracks emanating from the corners (l) of the indents were measured to calculate the fracture toughness. The dark voids are due to sample pullout and porosity. Reproduced with permission © (2013) Springer. Journal of Materials Science[32]

It was observed that the material exhibited a critical load of 0.5 kgf where spalling, as shown in Fig. 2.4, occurs and limits the ability to obtain accurate hardness measurements. Tests beyond this load were excluded in accordance with ASTM C1327-08 [30]. Vickers hardness values

for $La_{3-x}Te_4$ were measured up to 0.5 kgf, where the values approached a plateau of HV = 335 ± 6 kgf/mm^2 (0.5 kgf/10 s contact). For comparison, $La_{3-x}Te_4$ is not a hard ceramic when compared to SiC, a structural ceramic which has a hardness value of HV of ~2500 kgf/mm^2 and was closer to a glass HV of ~500-1000 kgf/mm^2 [35]. Materials with higher hardness values would be more resistant to surface defects during handling and operation, thus reducing the number of potentially fatal defects. However, $La_{3-x}Te_4$ was not a particularly hard ceramic and was observed to be brittle, thus reflecting the challenges of working with this particular material.

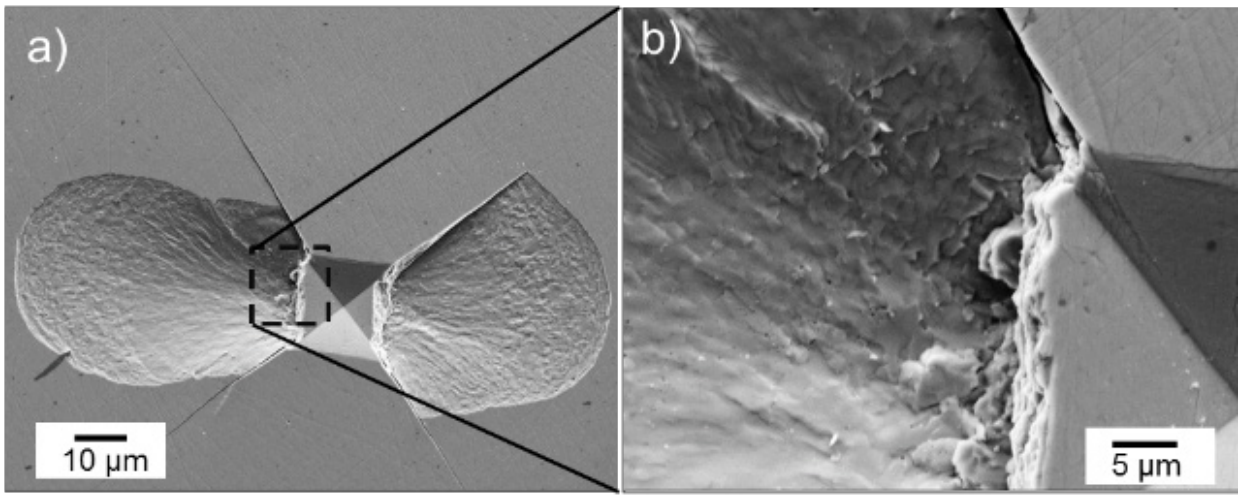

Figure 2.4 a) Scanning electron micrograph of a Vickers indent made under a load of 1.0 kgf. Spalling was observed to the left and the right of the indent image. This load corresponds with the transition from the Palmqvist regime of surface cracks to the half-penny regime which is a mixture of surface and radial cracks. The roughness of the fractured surface at the points furthest from the indent is indicative of intergranular fracture following grain boundaries **b)** A magnified view of where the indent meets the spalled surface. The smoothness of the fracture surface is mirror like and is indicative of transgranular fracture across grain boundaries. Reproduced with permission © (2013) Springer. Journal of Materials Science[32]

In comparison to other thermoelectric materials, $La_{3-x}Te_4$ is harder than Bi_2Te_3 HV = 63 kgf/mm^2 [27], silver and antimony doped PbTe at 0.3 kgf HV = 60-70 kgf/mm^2 [36], and PbTe at 0.01 kgf HV = 24 kgf/mm^2 [37]. It is comparable or slightly softer than the Skutterudite class of compounds at 0.1 kgf HV = 250-550 kgf/mm^2 which varies depending on the specific composition [38]. Although there is no reported hardness value for $Si_{0.8}Ge_{0.2}$,the hardness for bulk silicon is significantly higher in range of HV ~ 900 kgf/mm^2 [39].

$La_{3-x}Te_4$ exhibited a Vickers hardness indentation size effect (ISE), i.e. higher hardness values at lower indentation loads, a phenomenon that has been reported in microhardness testing for a wide range of metallic and ceramic materials [40]. Although there remains some controversy over the origin of the indentation size effect, the reader is referred to the following review papers for additional information [41–46]. Ideally, hardness values should be load independent (e.g. at high loads) or at least have the testing load specified to ensure proper comparison between materials systems. For $La_{3-x}Te_4$, the hardness value approaches ~340 kgf/mm^2 at the spalling limit and can be used as a basis for comparison. It has been previously reported that the brittleness of a material is inversely proportional to the load at which the onset of cracking occurs during indentation [47]. Therefore, rather than analyzing and reporting single load hardness values, it is useful that hardness testing be conducted at multiple loads to gain deeper insights into the mechanical behavior of thermoelectric materials.

For $La_{3-x}Te_4$, the onset of cracking was detected using the optical microscope at 0.05 kgf (although finer cracks have been detected at loads as low as 0.02 kgf using the scanning electron microscope) and correlates well with the region of sharply decreasing hardness values as seen in Fig. 2.2. This early onset of cracking indicates that the material is fairly brittle. However, due to

instrument limitations on indentation load step sizes, it was not possible to probe the samples at a sufficiently high resolution to determine the critical loads for the onset of crack formation. Nevertheless, these results agree with the observed apparent brittleness of $La_{3-x}Te_4$ during machining and handling of the material. $La_{3-x}Te_4$ follows the trend common for ionically bonded polycrystalline materials such that they tend to be brittle. Ionic bonding is generally rigid and resistant to plastic deformation resulting in brittle fracture as the dominate fracture mode [42]. The spalled surface shown in Fig. 2.4a reflects a mixture of transgranular and intergranular fracture. A magnified view of the spalled surface is shown in Fig. 2.4b. The region adjacent to the indent shows that the fractured surface is smooth and mirror-like which is characteristic of transgranular fracture. Further away from the indent, the surface exhibits a coarse texture and the roughness of the spalled area is likely due to the crack path following the texture of the grain boundaries. This trend reflects the mirror-mist behavior for brittle ceramics with the transition occurring as the crack velocity decreases away from the origin of failure [48]. With the limited viewing angles into the cracks emanating from the corners of the Vicker's indents, it is difficult to say exact nature of the fracture for the cracks. However since the spalling is related to the propagation of the cracks, it is plausible that the cracks follow the same mixed transgranular to intergranular behavior as the cracks extend further from the corner of the indent.

2.3.3 Vickers Indentation Fracture Toughness

Although issues have been raised concerning the accuracy and validity of using empirically derived correlation equations to calculate fracture toughness from Vickers indentation testing [49] , the calculated fracture toughness values were approximations given the

sample preparation difficulties in ASTM techniques. A review of the technique by Ponton and Rawlings suggests that the technique is a good approximation to within ~30% for unknown materials and serves as a rapid and convenient measurement technique when fabrication of ASTM test specimens is not possible[33,50]. Efforts are underway to enhance processing and machining capabilities to produce suitable ASTM materials, but given the current lack of capabilities to produce samples of suitable quality and the need for faster turnaround on mechanical properties, this technique is useful to provide semi-empirical data.

After considering nineteen different methods of analysis, Ponton and Rawlings[50,33] selected the equation developed by Shetty, Wright, Mincer, and Clauer for materials which exhibit cracking in the Palmqvist regime approximately l/a ≤ 3 [23]:

$$K_c = \frac{1}{3(1-\upsilon^2)(2^{1/2}\pi^{5/2}\tan\theta)}\left(\frac{H_v P}{4l}\right)^{1/2} \qquad (2)$$

where υ is the Poisson ratio, Θ is the indenter contact angle, H_v is the hardness at load P, a is the length of the 1/2 diagonal of the indent, and l is the edge crack length. The measured l/a for $La_{3-x}Te_4$ ranged from 1.6 to 3 with the value increasing with increasing load. The spalling in the material corresponds well with the transition from Palmqvist surface cracks to the half-penny median radial crack regime l/a > 3. Ponton and Rawlings generalized the equation by taking υ = 0.25, which is a good approximation for brittle materials, and Θ = 68° for a Vickers indent

$$K_C = 0.0319\frac{P}{al^{1/2}} \qquad (3)$$

Crack lengths for loads ranging from 0.05 kgf to 0.5 kgf were measured and are shown in Fig. 2.5. As noted before, errors in measurements at low loads arise due to difficulties in measuring small crack lengths using an optical microscope. At high loads, the tortuous nature of the crack paths leads to errors in crack length measurements. The crack lengths as a function of

load follow a linear relationship with $R^2 = 0.9965$. The linear relationship between crack length and indent load was also observed by Shetty, Wright, Mincer, and Clauer in WC-Co cermets [23].

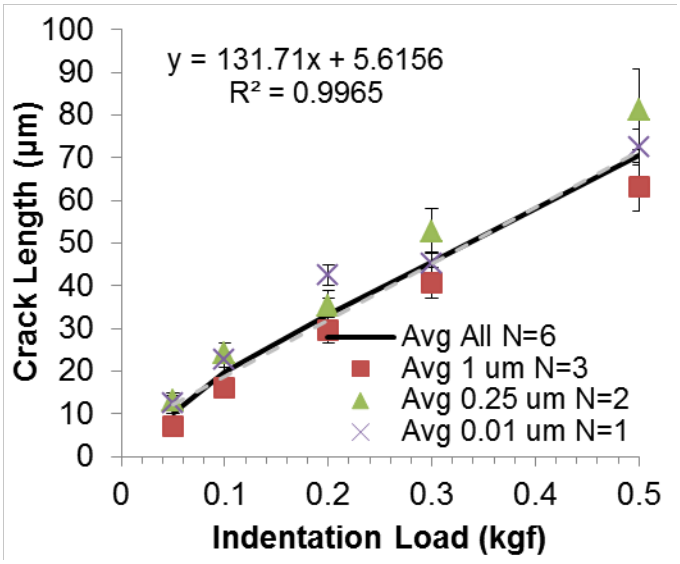

Figure 2.5 Average crack lengths for indentation loads between 0.05 kgf and 0.5 kgf. No cracks were observed below 0.05 kgf. Error bars represent 1 standard deviation. Reproduced with permission © (2013) Springer. Journal of Materials Science[32]

The calculated Vickers indentation fracture toughness is reported in Fig. 2.6. The values exhibit a subtle variation with $K_{VIF} = 0.68 \pm 0.17$ MPa-$m^{1/2}$ at low loads (0.05 kgf) to 0.71 ± 0.06 MPa-$m^{1/2}$ at high loads (0.5 kgf). The minimum dispersion in the data was observed at 0.3 kgf with $K_{VIF} = 0.70 \pm 0.06$ MPa-$m^{1/2}$. The lower error corresponds to a balance between the indent being sufficiently large, exhibiting long crack formation, and ideal linear crack formation. The cracks and indents at lower loads were difficult to measure using the optical microscope and at 0.5 kgf there was a breakdown from the idealized crack formation with crack branching and nonlinear cracks. Similar to the Vicker's hardness, the observed differences in fracture toughness

as a function of surface finish were within the limits of experimental error and the uncertainty of the SWMC model.

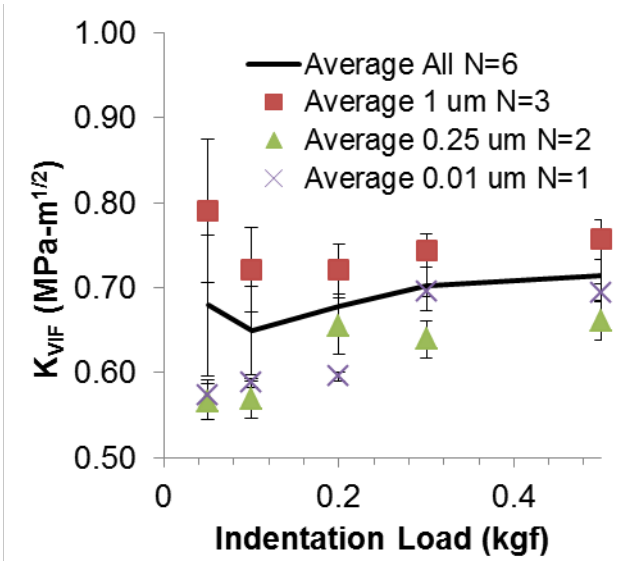

Figure 2.6 Vickers indentation fracture toughness K_{VIF} calculated from the measured crack lengths produced by Vickers indentations for $La_{3-x}Te_4$. No variation greater than the error measurement of K_{VIF} was observed as a function of surface finish within the limits of experimental uncertainty and the uncertainty of the correlation model. Error bars represent 1 standard deviation. Reproduced with permission © (2013) Springer. Journal of Materials Science[32]

The calculated fracture toughness corresponds well to the qualitatively observed brittle behavior of these materials. It is interesting to note that this value is comparable to the fracture toughness (K_{Ic}) of soda lime glass K_{IC} = 0.7 MPa-m$^{1/2}$ as measured through traditional techniques [51]. $La_{3-x}Te_4$ is more brittle when compared to other thermoelectric materials such as different compositions of the skutterudite class of thermoelectric materials that have fracture toughnesses of K_{IC} = 1.1-2.8 MPa-m$^{1/2}$ as determined by the Chevron V-notched beam test [13],

and K_{VIF} = 1.5-2.2 MPa-$m^{1/2}$ [38]. Bismuth telluride, Bi_2Te_3, also has a higher fracture toughness compared to $La_{3-x}Te_4$ with K_{VIF} values of 1.14 MPa $m^{1/2}$ [27]. However, $La_{3-x}Te_4$ is not as brittle as the PbTe-PbS materials with a reported K_{VIF} of 0.35 MPa-$m^{1/2}$ [52].

It is important to realize that at this stage of development it is very difficult to obtain samples of advanced thermoelectric materials which will satisfy ASTM specifications. Furthermore, these insights have allowed us to devise novel methods to obtain materials with enhanced mechanical behavior, thereby making this technique a useful tool for process optimization for a given material, as well as for comparisons between different classes of materials.

2.4 Conclusion

The Vickers hardness values have been measured for $La_{3-x}Te_4$ as a function of applied load. The indentation size effect is observed for this material and provides important information as to the brittleness of $La_{3-x}Te_4$. From crack measurements of the Vickers indents, the material possesses a fracture toughness value that reflects its brittle glass-like behavior. These values correlate with observations made from machining $La_{3-x}Te_4$ and suggest that the Vickers indentation technique is a useful tool in rapidly characterizing mechanical behavior. Although traditional ASTM K_{IC} techniques are advisable when possible, obtaining an approximate value through Vickers micro-indentation is useful and represents a practical balance considering the limitations in sample preparation for weak and brittle materials.

References

1. J. Yang and T. Caillat, *MRS Bull.*, 2006, **31**, 224–229.

2. J.-P. Fleurial, *JOM*, 2009, **61**, 79–85.

3. G. J. Snyder and E. S. Toberer, *Nat Mater*, 2008, **7**, 105–114.

4. *ASTM Stand. ASTM C1421 - 10 Stand. Test Methods Determ. Fract. Toughness Adv. Ceram. Ambient Temp.*, 2010.

5. *ASTM Stand. ASTM E1820 - 11 Stand. Test Method Meas. Fract. Toughness*, 2011.

6. *ASTM Stand. ASTM C1211 - 02 Stand. Test Method Flexural Strength Adv. Ceram. Elev. Temp.*, 2002.

7. *ASTM Stand. ASTM C 1499-09 Stand. Test method Monotonic Equibiaxial Flexural Strength Adv. Ceram. Ambient Temp.*, 2009.

8. J. R. Gladden, G. Li, R. Adebisi, S. Firdosy, T. Caillat, and V. Ravi, *Phys. Rev. B*, 2010, **82**, 1–6.

9. B. Duan, P. Zhai, P. Wen, and S. Zhang, *Scr. Mater.*, 2012, **67**, 372–375.

10. K. Ueno, A. Yamamoto, T. Noguchi, T. Inoue, S. Sodeoka, H. Takazawa, C. H. Lee, and H. Obara, *J. Alloys Compd.*, 2004, **384**, 254–260.

11. K. Ueno, A. Yamamoto, T. Noguchi, T. Inoue, S. Sodeoka, and H. Obara, 2005, **388**, 118–121.

12. K. Ueno, A. Yamamoto, T. Noguchi, T. Inoue, S. Sodeoka, and H. Obara, 2005, **392**, 295–299.

13. V. Ravi, S. Firdosy, T. Caillat, B. Lerch, A. Calamino, R. Pawlik, M. Nathal, A. Sechrist, J. Buchhalter, and S. Nutt, *AIP Conf. Proc.*, 2008, **969**, 656–662.

14. S. A. Firdosy, V. A. Ravi, B. Li, E. Brandon, T. Caillat, J.-P. Fleurial, K. Van Der Walde, L. Maricic, A. Pushko, and S. Nutt, .

15. S. Palmqvist, *Jernkontorets Ann.*, 1957, **141**, 300–307.

16. S. Palmqvist, *Arch. Eisenhuettenwes*, 1962, **33**, 629–634.

17. S. Palmqvist, *Jernkontorets Ann.*, 1963, **147**, 107–110.

18. B. Lawn and R. Wilshaw, *J. Mater. Sci.*, 1975, **10**, 1049–1081 LA – English.

19. B. R. Lawn and M. V Swain, *J. Mater. Sci.*, 1975, **10**, 113–122 LA – English.

20. A. G. Evans, in *Proceedings of the Eleventh National Symposium on Fracture Mechanics: Part IIo*, ASTM, 1979, pp. 112–135.

21. J. Lankford, *J. Mater. Sci. Lett.*, 1982, **1**, 493–495.

22. R. Spiegler, S. Schmauder, and L. S. Sigl, *J. Hard Mater.*, 1990, **1**, 147–158.

23. D. K. Shetty, I. G. Wright, P. N. Mincer, and A. H. Clauer, *J. Mater. Sci.*, 1985, **20**, 1873–1882.

24. K. Niihara, *J. Mater. Sci. Lett.*, 1983, **2**, 221–223.

25. J. J. Gilman, *Chemistry and Physics of Mechanical Hardness*, Wiley-Interscience, 2009.

26. A. G. Evans and E. A. Charles, *J. Am. Ceram. Soc.*, 1976, **59**, 371–372.

27. L.-D. Zhao, B.-P. Zhang, J.-F. Li, M. Zhou, W.-S. Liu, and J. Liu, *J. Alloys Compd.*, 2008, **455**, 259–264.

28. F. Ren, J. E. Ni, E. D. Case, J. Sootsman, M. G. Kanatzidis, E. Lara-Curzio, R. M. Trejo, E. J. Timm, and B. D. Hall, in *MRS Proceedings*, 2007, vol. 1044.

29. A. May, J. Fleurial, and G. Snyder, *Phys. Rev. B*, 2008, **78**, 1–12.

30. *ASTM Stand. ASTM C1327 - 08 Stand. Test Method Vickers Indentation Hardness Adv. Ceram.*, 2008.

31. *ASTM Stand. ASTM E122-10 Stand. Test Methods Determ. Aver. Grain Size*, 2010.

32. J. M. Ma, S. A. Firdosy, R. B. Kaner, J.-P. Fleurial, and V. A. Ravi, *J. Mater. Sci.*, 2014, **49**, 1150–1156.

33. C. Ponton and R. Rawlings, *Mater. Sci. Technol.*, 1989, **5**, 961–976.

34. W. L. Cox, H. Steinfink, and W. F. Bradley, *Inorg. Chem.*, 1965, **5**, 318–319.

35. in *CRC Materials Science and Engineering Handbook, Third Edition*, CRC Press, 2000.

36. F. Ren, E. D. Case, E. J. Timm, and H. J. Schock, *J. Alloys Compd.*, 2008, **455**, 340–345.

37. A. J. Crocker and M. Wilson, *J. Mater. Sci.*, 1978, **13**, 833–842.

38. G. Rogl and P. Rogl, *Sci. Adv. Mater.*, 2011, **3**, 517–538.

39. V. Domnich, Y. Aratyn, W. M. Kriven, and Y. Gogotsi, *Rev. Adv. Mater. Sci.*, 2008, **17**, 33–41.

40. G. M. Pharr, E. G. Herbert, and Y. Gao, *Annu. Rev. Mater. Res.*, 2010, **40**, 271–292.

41. G. Farges and D. Degout, *Thin Solid Films*, 1989, **181**, 365–374.

42. K. Sangwal, *Cryst. Res. Technol.*, 2009, **44**, 1019–1037.

43. J. Gong, J. Wu, and Z. Guan, *J. Eur. Ceram. Soc.*, 1999, **19**, 2625–2631.

44. J. Y. Shu and N. A. Fleck, *Int. J. Solids Struct.*, 1998, **35**, 1363–1383.

45. W. W. Gerberich, N. I. Tymiak, J. C. Grunlan, M. F. Horstemeyer, and M. I. Baskes, *J. Appl. Mech.*, 2002, **69**, 433.

46. a Gouldstone, N. Chollacoop, M. Dao, J. Li, a Minor, and Y. Shen, *Acta Mater.*, 2007, **55**, 4015–4039.

47. B. R. Lawn and D. B. Marshall, *J. Am. Ceram. Soc.*, 1979, **62**, 347–350.

48. G. D. Quinn, *Fractography of Ceramics and Glasses*, National Institute of Standards and Technology, 2007.

49. G. D. Quinn and R. C. Bradt, *J. Am. Ceram. Soc.*, 2007, **680**, 673–680.

50. C. Ponton and R. Rawlings, *Mater. Sci. Technol.*, 1989, **5**, 865–872.

51. S. M. Wiederhorn, *J. Am. Ceram. Soc.*, 1969, **1968**, 99–105.

52. J. E. Ni, E. D. Case, K. N. Khabir, R. C. Stewart, C.-I. Wu, T. P. Hogan, E. J. Timm, S. N. Girard, and M. G. Kanatzidis, *Mater. Sci. Eng. B*, 2010, **170**, 58–66.

Chapter 3: Equibiaxial Flexural Strength and Weibull Analysis of the Thermoelectric $La_{3-x}Te_4$

3.1 Introduction

Thermoelectric materials have been used in solid-state energy conversion devices that have demonstrated exemplary reliability and longevity. The devices are able to directly convert a heat gradient into electrical power through the Seebeck effect. Thermoelectric generators have been utilized with great success in deep space missions such as Voyagers 1 and 2 with sustained operation since 1977 [1,2]. The advent of new high efficiency thermoelectric materials have expanded possibilities to increase payloads, decrease costs, and facilitate their use in terrestrial applications such as waste heat recovery [2–4].

A challenge in the development of state-of-the-art thermoelectrics is that the materials often behave as weak, brittle ceramics. Legacy materials such as $Si_{0.8}Ge_{0.2}$ often exhibit greater strength and durability, which more closely resembles the mechanical behavior of structural ceramics [1]. However, modern high-efficiency thermoelectric materials tend to be weak and brittle, which presents significant challenges during manufacturing device components. Furthermore, there can be significant thermal stresses during operation as the temperature differential can often be several 100 K between the hot and cold junction of a thermoelectric element [5]. Therefore, a mechanically robust thermoelectric material is desirable to simplify handling during manufacturing, improve device yield, and to increase tolerance to the thermomechanical stresses encountered during operation.

3.2. Theory

3.2.1 Ring-on-Ring Testing Geometry for Measurement of Flexural Strength

The mechanical behavior of thermoelectric materials is analogous to brittle ceramics. Failure in ceramics is typically due to tensile stresses, but the low tensile strength and brittleness of ceramics often prevents use of standardized testing methods such as ASTM E8, which is commonly used for metals [6]. Flexural tests are typically used to characterize the strength of ceramic materials. Typically, the 3-point or 4-point bending geometry is used to test the flexural strength of a material. Samples are machined into long rectangular bars and placed in a test fixture with two rollers that support the sample. Depending on the geometry, one or two rollers then apply a load to the sample causing it to bend. The side closest to the loading surface experiences compressive forces and the side away from the loading surface experiences tensile forces. The point of origin for failure occurs on the tensile surface away from the loading surface. However, due to difficulties in machining, the ring-on-ring geometry is an attractive alternative for determining the flexural strength of thermoelectric materials [7]. It is relatively straightforward to create cylinders of thermoelectric materials through uniaxial hot pressing or spark plasma sintering from cylindrical dies. The ingots are then cut into discs and polished for testing. In comparison, a geometry for 4-point flexural test specimens are 2.0 mm x 1.0 mm x 25 mm and are challenging to produce with sufficient quality [8]. The ring-on-ring testing geometry has been used effectively in testing of other brittle materials for similar reasons, thus reducing the complexity and cost associated with manufacturing a sufficient number of samples to provide a statistically significant measure of flexural strength [9–14].

In equibiaxial flexural testing, the sample rests upon a larger diameter support ring and a smaller diameter load ring applies a uniform stress to the top of the sample. The flexural strength can be calculated using Equation 1:

$$\sigma_f = \frac{3F}{2\pi h^2}\left[(1-\upsilon)\frac{D_S^2 - D_L^2}{2D^2} + (1-\upsilon)\ln\frac{D_S}{D_L}\right] \quad (3.1)$$

where σ_f is the flexural strength, h is the thickness of the sample, υ is Poisson's ratio, D_s is the diameter of the support ring, D_L is the diameter of the load ring, and D is the diameter of the test specimen [7]. For $La_{3-x}Te_4$, υ = 0.22 as determined by resonance ultrasound spectroscopy [15] and is fairly typical for a brittle ceramic material. Furthermore, from ASTM C 1499 [7], it should be noted that the error in flexural strength is less sensitive to errors in υ when an appropriate estimate is used.

3.2.2 Failure in Brittle Ceramics

The strength of a polycrystalline ceramic is strongly dependent upon the population of flaws in the material. The origin of failure is due to a critical strength limiting flaw which include such defects such as porosity, secondary phases, surface flaws, *etc*. [16]. The flaws act as stress concentrators which give rise to crack formation and ultimately failure. The existence of some variation of these flaws is inherent in all ceramics, making characterization of these flaws the first step toward mitigation to improve material strength. The flaws can be located on the surface of the test specimen and/or internally (volume) distributed. The population and severity of surface flaws can be reduced with improved machining, careful handling, surface chemical treatments, *etc.* of the test specimens. However, volume distributed flaws are more complex and

require adjustments to the processing conditions such as particle size, milling parameters, synthetic procedures, powder purity, pressing conditions, porosity, *etc.* Careful analysis of the nature of flaws is thereby important for identifying potential avenues to improve mechanical performance.

Brittle thermoelectric materials are highly sensitivity to flaws because of their low resistance to fracture also known as fracture toughness, K_{IC}. Polycrystalline thermoelectric materials to a first approximation follow the Griffith brittle crack theory. Once a crack is initiated, the energy of crack propagation is proportional to the energy for formation of new surfaces. Therefore, only modest stress is needed to cause catastrophic failure once a crack is initiated, since there are few low energy means, such as dislocation movement or plastic deformation, to alleviate the stress. As a consequence, the sensitivity to flaw population makes testing of ceramics difficult as samples are highly dependent upon processing history and a given material can have significant variations in strength due to statistical distributions of flaws in a material. Therefore, having a good understanding of the strength distribution of a ceramic is essential for the design of thermoelectric devices.

3.2.3 Distribution of Strength in Ceramics

One way to understand the distribution of strength in a ceramic is the Weibull probability distribution function. The Weibull function is applicable to systems characterized by their "weakest-link" and is extensively used in lifetime failure analysis [17]. The Weibull probability distribution function has been shown to be appropriate for describing the mechanical behavior of brittle materials because a dominant strength-limiting flaw will serve as the "weakest link" in the

material and result in catastrophic failure [18]. A useful form of the probability distribution function is the 2-parameter Weibull equation [17]:

$$F = 1 - \exp\left(-\left(\sigma_f / \sigma_0\right)^m\right) \tag{3.2}$$

where F is the probability of failure, σ_f is the flexural strength, σ_0 is the characteristic strength, and m is the Weibull modulus. The Weibull modulus m, also known as the shape parameter, describes the shape of the distribution function and is inversely proportional to the scatter in strength. It is therefore desirable to have both high values for σ_0 and m so that a material will have high strength as well as high reliability [17].

The 2-parameter Weibull distribution function can be linearized by taking the double natural logarithm of the function to obtain:

$$\ln\left(\ln\left(1/(1-F)\right)\right) = m\ln(\sigma_f) - m\ln(\sigma_0) \tag{3.3}$$

The characteristic strength can then be determined by setting the strength of failure equal to the characteristic strength, $\sigma_f = \sigma_0$. From the mathematics, the characteristic strength σ_0 is defined as the point where 63.2% of the population is expected to fail. The σ_0 parameter is also known as the scale parameter and helps define the position of the distribution function on the strength scale.

The Weibull distribution for a population of samples can be determined by first measuring the flexural strength of each sample in that population. Next, the data can be fit to Equation 3 by ranking the sample set in order of increasing flexural strength. The failure probability for the population can be estimated using Equation 4 [19]:

$$F = (I - 0.5)/N \tag{3.4}$$

where I is the rank of the sample and N is the total number of samples. Utilizing a linear least square regression fit to the data and Equation 3, the slope and y-intercept can be used to calculate m and σ_0, respectively.

The parameters σ_0 and m for a thermoelectric material can be used, in conjunction with thermomechanical finite element modeling, to design reliable thermoelectric devices with minimal failure probability for the duration of device operations. Furthermore, the Weibull analysis can be utilized to understand and implement processing and/or materials improvements. In this study, the high temperature n-type thermoelectric material $La_{3-x}Te_4$ was investigated because of its relevance to the next generation of thermoelectric generators under development at the Jet Propulsion Laboratory [20, 21]. $La_{3-x}Te_4$ has the highest reported bulk n-type thermoelectric figure of merit, zT = 1.2 at 1273 K. The figure of merit zT is defined as $zT = S^2T/\rho\kappa$ where S is the Seebeck coefficient, ρ is the electrical resistivity, and κ is the thermal conductivity. $La_{3-x}Te_4$ possesses a defect structure with its carrier concentration controlled by the La vacancy concentration. The hardness and Vicker's indentation fracture toughness of lanthanum telluride have been recently reported [22]. Gaining insights into the flexural behavior of this material is important to ensure proper component design and to serve as a comparison baseline for understanding improvements in processing and materials strength.

3.3 Experimental

Samples of $La_{3-x}Te_4$ with the nominal composition of x = 0.23 were produced using the powder metallurgical techniques outlined by A. May, *et al*. [20]. The powder was consolidated through uniaxial hot pressing to 12.56 mm diameter cylinders with >98% theoretical density as determined through geometric density measurements. Samples were cut into discs using a high

precision diamond abrasive saw to ~1.5 mm and then ground to the nominal dimensions of 12.56 mm dia x 1.00 mm. The samples were polished on both sides to the final dimensions by sequential grinding using 240, 320, 400, 600, 800, and 1200 grit SiC polishing papers, which resulted in a highly reflective final finish with a surface roughness of R_a = 0.25 μm.

The equibiaxial flexural strength was measured following procedures outlined in ASTM C 1499-09 Standard Test method for Monotonic Equibiaxial Flexural Strength of Advanced Ceramics at Ambient Temperature [3]. The test fixture was supplied by Wyoming Test Fixtures with a support ring diameter D_s = 10 mm and the loading ring diameter D_L = 4 mm. Mechanical tests were conducted using an Instron 5562 test frame with a 500 N load cell at a crosshead speed of 0.095 mm/min in accordance with ASTM C 1499-09. Samples were examined using optical and electron microscopy.

3.4. Results

3.4.1 Flexural Strength

The prepared samples were visually inspected for edge flaws and other defects prior to testing. Samples were rejected if surface defects were significant and could not be removed with additional polishing. After testing, the samples were subsequently inspected with an optical microscope and rejected if the failure patterns fail to meet the guidelines outlined in the ASTM C 1499 [7]. In this study, one sample was rejected after testing due to an irregular fracture pattern as shown in Fig. 3.1. The sample failed outside of the loading ring and was excluded because the points of highest stress should be located within the loading ring in the equibiaxial geometry.

A series of N = 29 samples were measured with average flexural strength $\bar{\sigma}_f$ = 31.4 MPa with a standard deviation of ± 8.9 MPa. There was significant scatter in the data with the coefficient of variation = 29%, which is fairly typical for brittle ceramics [23]. The samples were ranked in terms of failure strength in accordance with Equation 4 and the distribution of strengths was analyzed using the Weibull distribution function through fitting to Equation 3.

The Weibull plot of the samples and the fit to Equation 3 is shown in Fig. 3.2. The fit has an R^2 = 0.976 indicating that the failure of $La_{3-x}Te_4$ follows Weibull statistics well [17]. From the linear least square regression analysis, the Weibull parameters of characteristic strength σ_0 = 34.5

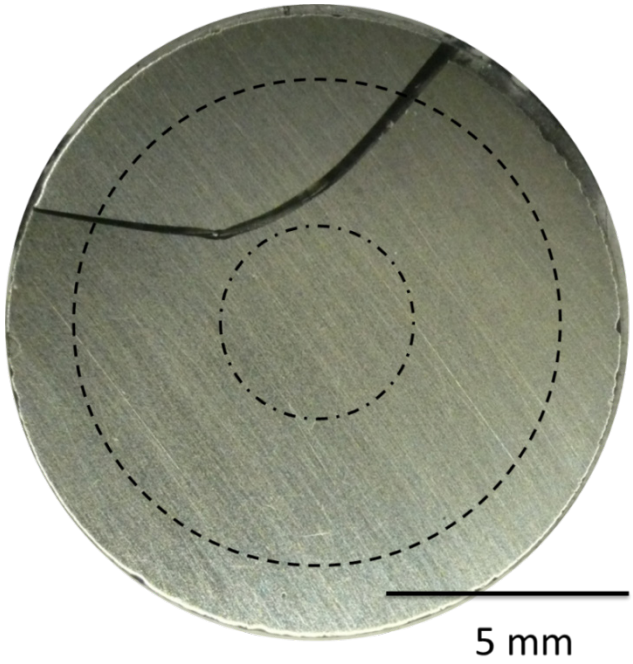

Figure 3.1 Example of sample rejected due to the fracture path occurring outside of the load ring.

MPa and the Weibull modulus m = 4.2, were determined. Furthermore, the fit to a single slope suggests that there is a dominant failure probability distribution which governs the strength of this material [17]. The types of flaws that make up the defect population and the severity of the defects in the material are further examined in a later section.

The failure probability plot as a function of applied stress for $La_{3-x}Te_4$ is shown in Fig. 3.3. The fitted curve was generated from the calculated σ_0 and m with an overlay of experimental data. The relatively low Weibull modulus indicates that there is a large spread in the failure strengths for $La_{3-x}Te_4$ which is represented as the broadened S-shape of the failure probability plot. In comparison, the legacy high temperature thermoelectric material $Si_{0.8}Ge_{0.2}$ is significantly stronger. The maximum flexural stress (±20%) for p-type and n-type materials are $\bar{\sigma}_f$ = 201 and $\bar{\sigma}_f$= 129 MPa, respectively [1]. To improve thermal-to-electrical conversion efficiency, $La_{3-x}Te_4$

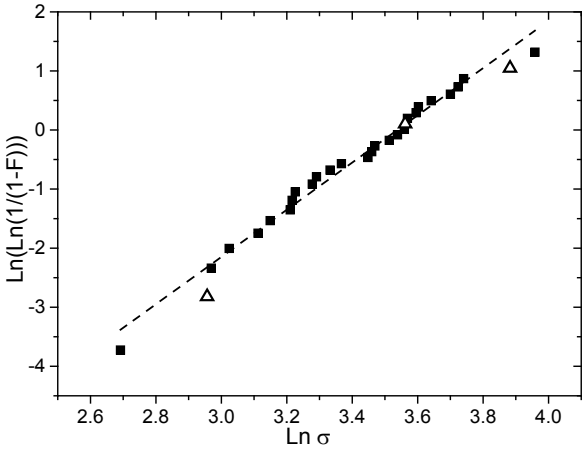

Figure 3.2 Plot of Equation 3 with a line fit to determine the Weibull modulus and characteristic strength. Hollow triangles represent the low, medium, and high strength failure samples from Figs. 4-6.

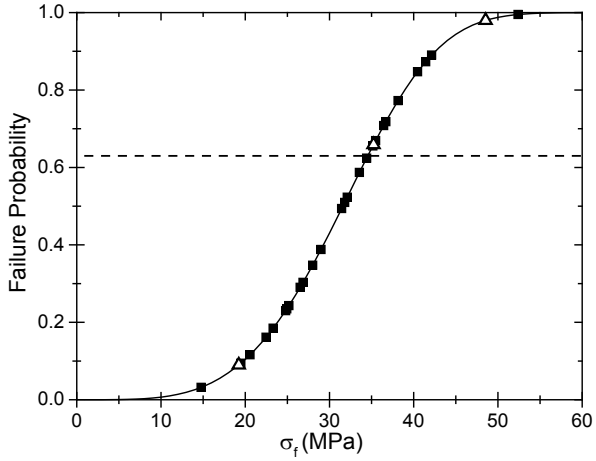

Figure 3.3 Flexural strength failure probability curve as determined from the Weibull parameters fit. The 63.2% probability, which defines the characteristic strength, is shown as the horizontal dashed line. Hollow triangles are the low, medium, and high strength failure samples from Figs. 4-6.

can be segmented with the skutterudite class of thermoelectric materials which has a peak zT at a lower temperature. The flexural strength and Weibull parameters of p-type skutterudite of the composition used were $\bar{\sigma}_f$ = 37.3 ± 6.7, σ_0 = 40, m = 5.64. The flexural strengths and Weibull parameters of the n-type skutterudite composite were measured to be and $\bar{\sigma}_f$ = 85.5 ± 13.3, σ_0 = 91 MPa, m = 7.29 [24]. Salvador *et al.* have reported on the flexural strength for a skutterudite with a different composition to be σ_0 = 123 MPa and m = 3.4 [25]. Therefore, when producing a segmented thermoelectric device with a skutterudite to improve the average zT, $La_{3-x}Te_4$ will be the mechanically weaker segment and more susceptible to failure.

3.4.2 Fractography

To better understand the strength limiting flaws, a series of samples were examined through microscopy. First, the tensile surface and cross-section were analyzed utilizing optical microscopy. Next, back scattered electron (BSE) images were obtained using scanning electron microscopy (SEM) to examine for phase inhomogeneity and grain morphology. An example of low strength, medium strength, and high strength failure modes are shown in Figs. 3.4-3.6. A clear feature in all of the samples is the cantilever curl seen on the edges of the compressive face of each sample. The cantilever curl is characteristic of flexural testing and is attributed to the change in crack path direction due to decreasing crack velocity as the crack moves away from the crack origin on the tensile surface [16].

For all test specimens, the mirror zone for $La_{3-x}Te_4$ is larger than the sample dimensions. This is common for materials with low flexural strengths and makes identifying the fracture origin difficult as there are no clear defining characteristics such as hackle lines or a mirror-mist zone which definitively point toward a fracture origin [16]. However, there are observable features in optical micrographs of the fracture surfaces which suggest the likely location of the failure origin. As can be seen in Figs. 3.4-3.6, the black arrow in the optical micrograph of the fractured cross-section marks the tensile surfaces near the centers of the sample within the loading ring area, which suggests a fracture origin. From the optical micrographs alone, it is inconclusive whether the cracks originate from a surface defect or a near surface defect. Only through closer examination through SEM could the flaws be identified as volume distributed flaws. Furthermore, analysis of the flaws suggests that there are 3 dominant volume dispersed flaw types in the material.

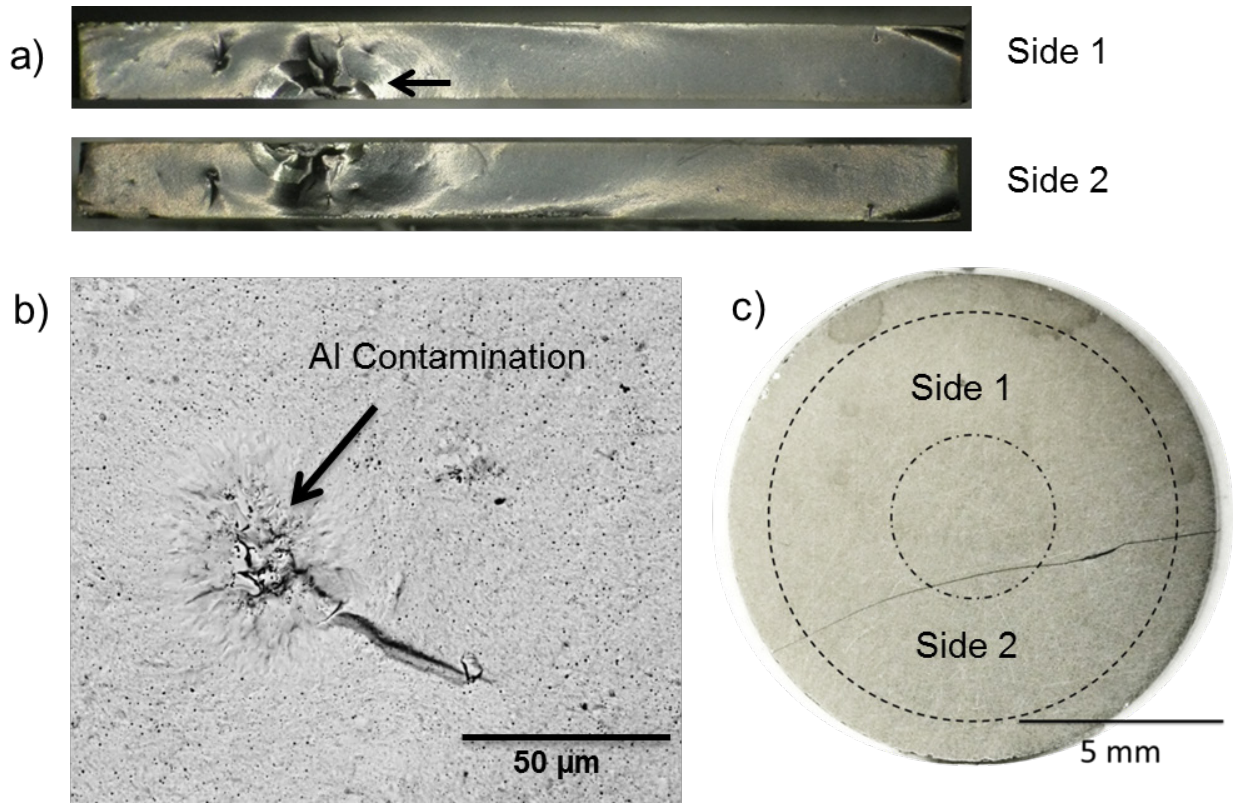

Figure 3.4 Example of low strength failure: a) Optical micrograph of a fractured cross-section with the failure origin indicated by the black arrow. Tensile surfaces from Side 1 and 2 face each other. b) Backscattered electron image of the failure origin. Aluminum contamination as determined by EDS. c) Plan view of the tensile surface with an overlay of the loading (inner) and support (outer) rings.

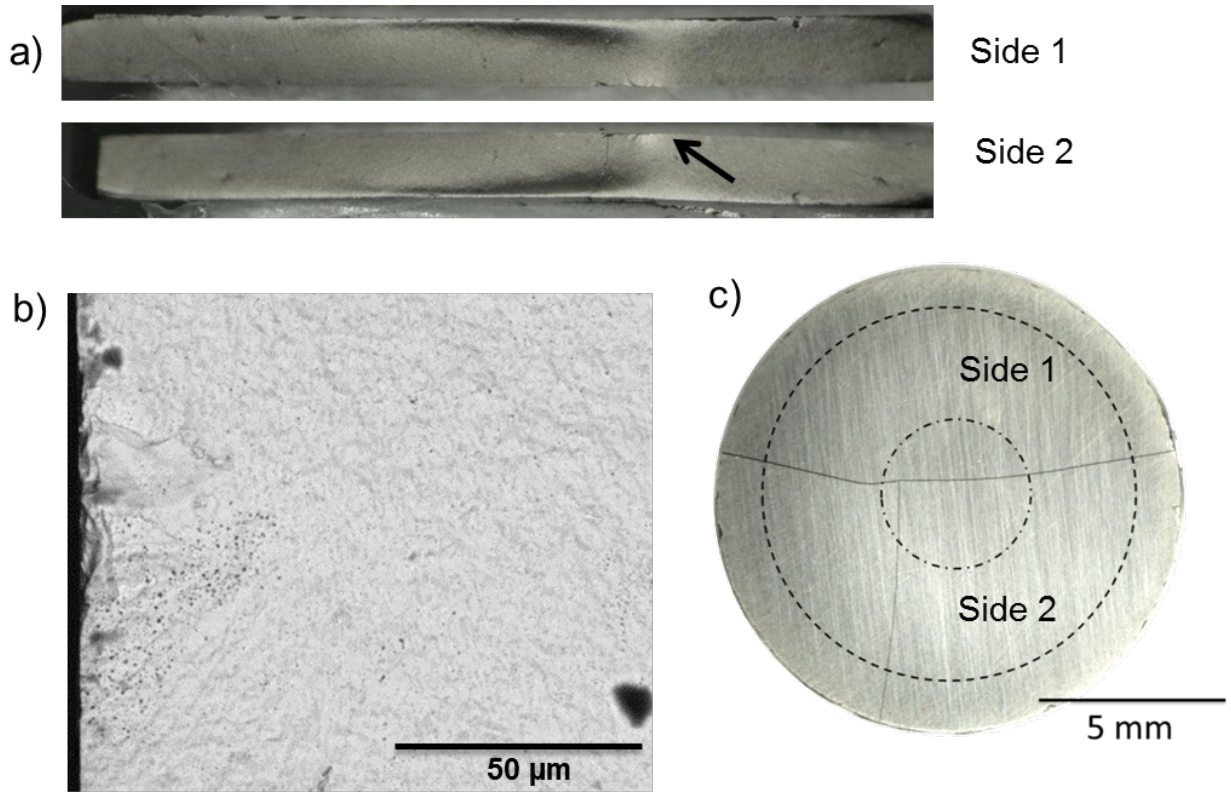

Figure 3.5 Example of medium strength failure: a) Optical micrograph of a fractured cross-section with the failure origin indicated by the black arrow. Tensile surfaces from Side 1 and 2 face each other. b) Backscattered electron image of the failure origin. No contaminants are observed, but there is evidence of agglomerated pores near the tensile surface (left), which could be the critical flaw. c) Plan view of the tensile surface with an overlay of the loading (inner) and support (outer) rings.

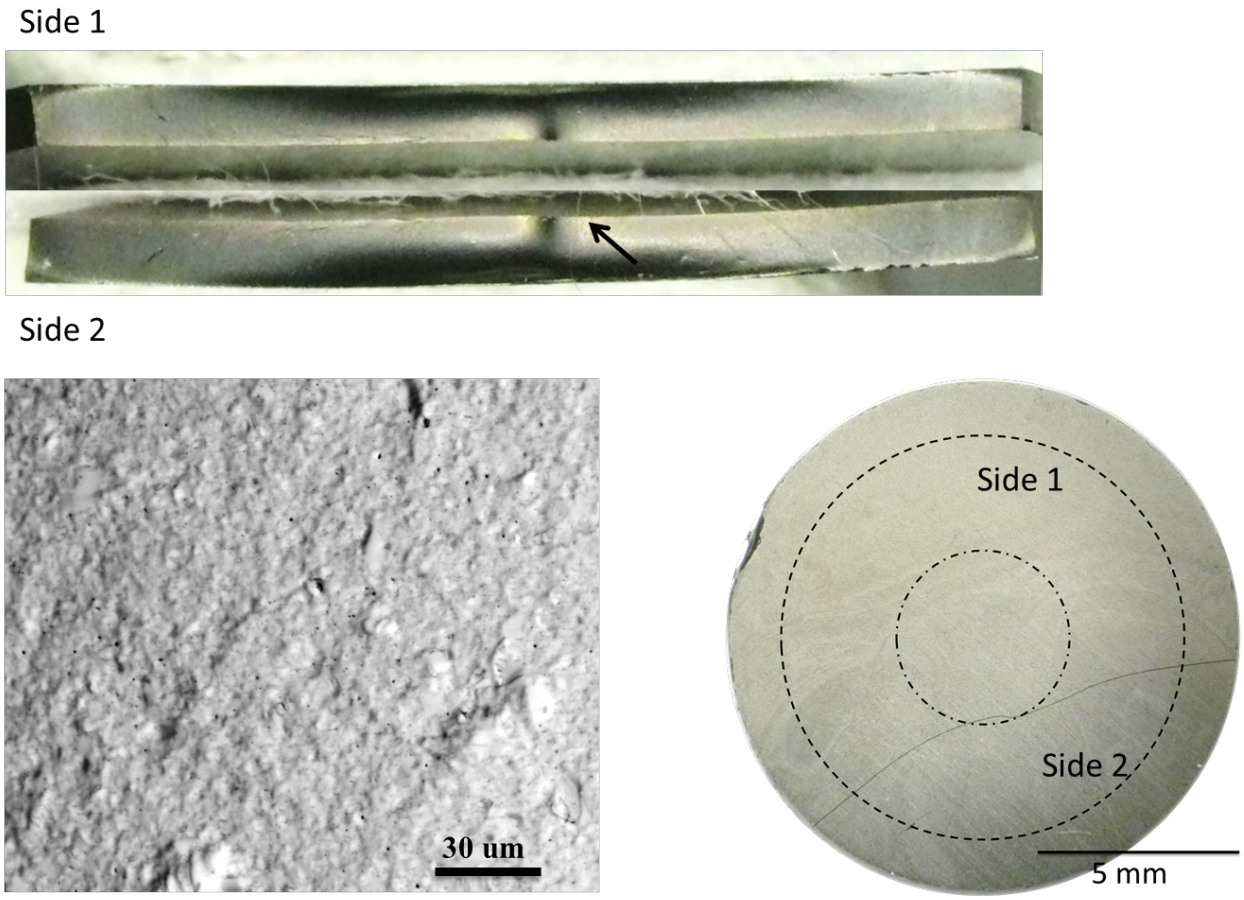

Figure 3.6 Example of high strength failure: a) Optical micrograph of a fractured cross-section with the failure origin indicated by the black arrow. Tensile surfaces from Side 1 and 2 face each other. b) Backscattered electron image near the failure origin. The grain structure is smooth and relatively free of pores and secondary phases which could explain the high strength of this material. c) Plan view of the tensile surface with an overlay of the loading (inner) and support (outer) rings.

3.4.3 Phase Inhomogeneity

Phase inhomogeneity is a byproduct of the powder metallurgical process used to produce $La_{3-x}Te_4$. A challenge in the synthesis of $La_{3-x}Te_4$ is that tight stoichiometric control is needed to control carrier concentration. May *et al*. showed that ball milling was advantageous over traditional melt processing techniques, which had difficulties with the high vapor pressure of Te and incongruent melting [20]. However, a byproduct of ball milling is contamination from the milling vessel and milling media. An example of failure likely due to an impurity phase is shown in Fig. 3.7. The darker region as determined from energy dispersive X-ray spectroscopy (EDS) is a mixture of Fe/Cr, likely from the stainless steel ball milling vial and/or balls. Near the inclusion particles, it is observed that there is a higher population of pores, which may be an indication of poor sintering due to the mismatch in the coefficient of thermal expansion [26]. Optimization of milling parameters can reduce contamination, but it is difficult to fully eliminate contamination due to the milling process.

A different source of contamination is observed in Fig. 3.4. In the example of low strength failure, the material exhibited aluminum contamination as determined through EDS. A potential source of the contamination is the Al_2O_3 abrasive used to clean the ball milling vials between batches. Again, there appears to be a chemical reaction or thermal expansion mismatch between the matrix and the contaminant particle, which is deleterious to the mechanical performance of this sample. The presence of this contaminant is likely avoidable with more careful cleaning of the milling vessel after abrasive cleaning.

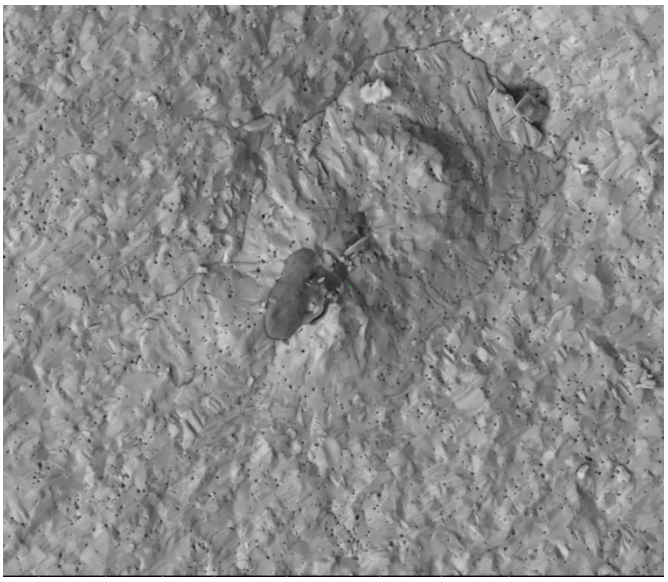

Figure 3.7 Backscattered electron image of a fractured cross-section of $La_{3-x}Te_4$. The dark area in the center of the image was determined to be Fe/Cr through EDS, which is likely to be contamination from ball milling in the stainless steel vials. The phase impurity and enhanced cracking suggest that this impurity may be the strength-limiting flaw.

Both Fe/Cr and Al contaminants appear to have a detrimental effect on material strength. Although Al contaminants can be eliminated through better cleaning procedures, it is unlikely that Fe contaminants will ever be completely eliminated because the Fe-based milling containers and media used in ball milling. It is likely that samples with higher populations of Fe/Cr particles produced the lower observed strengths in the Weibull distribution. Reduction in milling times and energies could possibly reduce the number of Fe/Cr particles, but this needs to be balanced with ensuring that the reaction goes to completion.

3.4.4 Porosity

Porosity is a feature present in all of the samples which were determined to be >98% of the theoretical density based on geometric measurements. A small amount of residual porosity in the samples can be seen in the SEM micrographs of the fractured cross-sections shown in Figs. 3.4-3.6. Porosity is present as submicrometer circular dark spots in the micrographs. The majority of pores are randomly dispersed throughout the material. However, a key feature is that pores accumulate near defects such as in phase inhomogeneities that can be seen in Figs. 3.4 and 3.7.

Pores increase the stress intensity factor which can lead to crack initiation [16]. However, it is difficult to attribute the failure origin to any particular porous region in the sample without more definitive fractographic features. In addition, porous seams and aggregates such as those seen in the left edge of the SEM micrograph in Fig. 3.5, can be the failure origin itself. These seams are a feature of the sintering and can be difficult to eliminate without drastic modifications to the hot pressing parameters. In the example of medium strength failure shown in Fig. 3.5, no secondary phase was observed in the SEM and it is possible that the pore clusters are the strength-limiting defect. In the example of high strength failure in Fig. 3.6, these porous clusters are not observed and the pores appear to be more randomly distributed. The absence of pore clusters could explain the higher observed strength for this sample.

The nature and extent of flaw populations dictate the magnitude and distribution of the strength of brittle materials such as lanthanum telluride. Comparing the SEM fractographs of the low strength, medium strength, and high strength failure samples in Figs. 3.4-3.6, the high strength failure sample had no observed secondary phases or pore agglomerates in the fractured

surface of the sample near the failure origin. This is in contrast to the low strength failure seen in Fig. 3.4 with a contaminant particle and the medium strength failure in Fig. 3.5 with the porous seams along the tensile surface of the fractured cross-section. This suggests that minimizing the flaw population will increase the strength of the material. These observations also suggest that particular flaws are more detrimental to the mechanical behavior of the material. Secondary phase contaminants which are chemically reactive and/or poorly matched to the coefficient of thermal expansion of $La_{3-x}Te_4$ will be more detrimental to strength compared to porosity. This finding suggests that greater improvements in strength can be achieved by reducing the level of contaminants in the starting powder compared to improving sintering.

3.5. Summary

The equibiaxial flexural strength of $La_{3-x}Te_4$ has been characterized and the failure strengths of $La_{3-x}Te_4$ have been shown to fit a Weibull distribution. $La_{3-x}Te_4$ is a comparatively weak thermoelectric material with a wide spread in strength values. Despite this, thermoelectric devices have been successfully fabricated using lanthanum telluride. However, as seen by the possible failure mechanisms, there is an opportunity for processing improvements of this material to enhance mechanical strength. Significant improvements to the mechanical performance will likely require the exploration of ceramic strengthening techniques to boost the mechanical properties of this high zT material.

References

[1] Vining CB. Silicon Germanium, in: Rowe DM (Ed.). CRC Handb. Thermoelectr., vol. 2. 1995.

[2] Fleurial J-P. JOM 2009;61:79.

[3] Snyder GJ, Toberer ES. Nat Mater 2008;7:105.

[4] Yang J, Caillat T. MRS Bull 2006;31:224.

[5] Firdosy SA, Li B, Brandon E, Caillat T, Fleurial J, Walde K Van Der, Pushko A, Nutt S, Ravi VA. 11th Int Energy Convers Eng Conf 2013:1.

[6] ASTM E8/E8M - 13a Standard Test Methods for Tension Testing of Metallic Materials, in: ASTM Vol. 03.01 Met. -- Mech. Testing; Elev. Low-Temperature Tests; Metallogr. ASTM International; 2013.

[7] ASTM Stand ASTM C 1499-09 Stand Test method Monotonic Equibiaxial Flexural Strength Adv Ceram Ambient Temp 2009.

[8] ASTM Stand ASTM C1211 - 02 Stand Test Method Flexural Strength Adv Ceram Elev Temp 2002.

[9] Ritter JE, Jakus K, Batakis A, Bandyopadhyay N. J Non Cryst Solids 1980;38-39:419.

[10] Fessler H, Fricker D. J Am Ceram Soc 1984;67:582.

[11] Nie X, Chen WW, Templeton DW. Int J Appl Ceram Technol 2010;7:616.

[12] Salem JA, Nemeth NN, Powers LM, Choi SR. Reliability Analysis of Uniaxially Ground Brittle Materials. 1995.

[13] Salem J, Jenkins M. Exp Tech 1999:19.

[14] Wereszczak A, Kirkland T, Breder K. Int J Microcircuits Electron Packag 1999;22:446.

[15] Gladden JR, Li G, Adebisi R, Firdosy S, Caillat T, Ravi V. Manuscr Prep n.d.

[16] Quinn GD. Fractography of Ceramics and Glasses. National Institute of Standards and Technology; 2007.

[17] Abernethy RB. The New Weibull Handbook, 2nd Editio. North Palm Beach, FL: Robert B Abertnathy; 1996.

[18] Klein CA, Miller RP, Gentilman RL. Opt Eng 2002;41:3151.

[19] ASTM C 1239-7 Stand Pract Report Uniaxial Strength Data Estim Weibull Distrib Parameters Adv Ceram 2007:1.

[20] May A, Fleurial J, Snyder G. Phys Rev B 2008;78:1.

[21] Bux S, Fleurial J-P, Caillat T, Li BY, Star K, Firdosy S, Ravi V, Huang C-K, Cheng B, Gogna P, Ma JM, von Allmen P, Vo T. 11th Int Energy Convers Eng Conf 2013.

[22] Ma JM, Firdosy SA, Kaner RB, Fleurial J-P, Ravi VA. J Mater Sci 2014;49:1150.

[23] Ring TA. Fundamentals of Ceramic Powder Processing and Synthesis. 1996.

[24] Ravi V, Firdosy S, Caillat T, Lerch B, Calamino A, Pawlik R, Nathal M, Sechrist A, Buchhalter J, Nutt S. AIP Conf Proc 2008;969:656.

[25] Salvador JR, Yang J, Shi X, Wang H, Wereszczak AA, Kong H, Uher C. Philos Mag 2009;89:1517.

[26] May A, Snyder J, Fleurial J. Sp Technol Appl Int Forum 2008:672.

Chapter 4: Improved zT in Percolated $La_{3-x}Te_4$-Ni Composite

4.1 Introduction to Thermoelectric Composites

The efficiency of a thermoelectric device is directly related to the ΔT, hot junction temperature, and material thermoelectric figure of merit, $zT = S^2T/\rho k$, where S is the Seebeck coefficient, ρ is the electrical resistivity, κ is the total thermal conductivity, and T is the absolute temperature. These properties are interconnected and improvement in one property generally leads to diminishment of another. As a result, the zT for most thermoelectric materials have remained relatively low, limiting thermoelectrics to niche applications such as in space.

As a result of the coupled transport properties, the strategy to develop thermoelectric composites to combine the properties of dissimilar materials comes as a straightforward consequence. The ideal thermoelectric would combine the low resistivity of a metal, the low thermal conductivity of a glass, and the Seebeck coefficient of an insulator. However, in practice it has been difficult to separate the individual transport properties of each component phase and combine them in a favorable manner as a composite material. The challenge of composites is further complicated by the potential for chemical reaction between phases and the possible coarsening of inclusions during operation resulting in instability of transport properties.

Due to the complexities of utilizing composites, previous efforts by others have focused on using nanoscale inclusions on the order of the phonon wavelength to cause phonon scattering[1,2]. However, one of the challenges of thermoelectric materials is that long-term high-temperature operations can result in grain growth that reduces performance. Recently, there have been several reports of high zT in materials such as PbTe-PbS[3], Si nanowires[4,5], etc., but these

materials require complex fabrication and/or are unable to function at higher temperatures where the efficiency improves.

4.2 Theoretical Calculations Indicate the Possibility of Improving the Power Factor

Therefore it is still desirable to combine the properties of dissimilar materials in a composite that can avoid potential problems of grain growth, improve the power factor (S^2/ρ) and/or be used in conjunction with nano-inclusions to further enhance zT. Initially, Bergman and Levy modeled a composite thermoelectric as an isotropic material and calculated that a composite would not have a zT larger than any phase[6]. However, upon refinement of the model, Bergman and Fei found that it was theoretically possible to improve upon the power factor of a composite under certain composite geometries of parallel slabs, parallel rods, or core/shell particles[7]. These ordered geometries are complex to synthesize and would be difficult to scale.

It would be ideal to utilize these concepts to improve the power factor without requiring the complex synthesis. Here we describe a scalable method to produce a bulk high-temperature high-zT thermoelectric composite. It draws upon some of the conclusions from Fei and Bergman that it would be possible to increase the power factor in a system with a good thermoelectric material with inert metallic inclusions with the same sign for the Seebeck coefficient[7].

4.3 Methods Summary

$La_{3-x}Te_4$ with the nominal composition of x = 0.23 was produced using a procedure outlined by A. May, et al.[8]. For this study, the same parent batch of $La_{3-x}Te_4$ was used for examining the effect of the Ni loading fraction to ensure that the material all started with the same carrier concentration. The $La_{3-x}Te_4$ powder was blended with nickel powder (Alfa Aesar

2.2-3.0 μm) in a Spex Mixer Mill under inert atmosphere and the powder mixture was consolidated using spark plasma sintering at 1350 ^{o}C and 80 MPa. Measurement of transport properties were carried out using techniques outlined elsewhere[9].

4.4 Results of Percolated $La_{3-x}Te_4$-Ni Composites

We start with a high-temperature high-zT thermoelectric and improve upon the zT by combining it with a metal which forms a low resistivity percolated network. The base thermoelectric material is $La_{3-x}Te_4$, an n-type high temperature thermoelectric material with a previously reported zT = 1.2 @ 1273 K[8,10] and through compositing we are able to achieve a 50% improvement with zT = 1.8 @ 1273 K (Fig. 4.1).

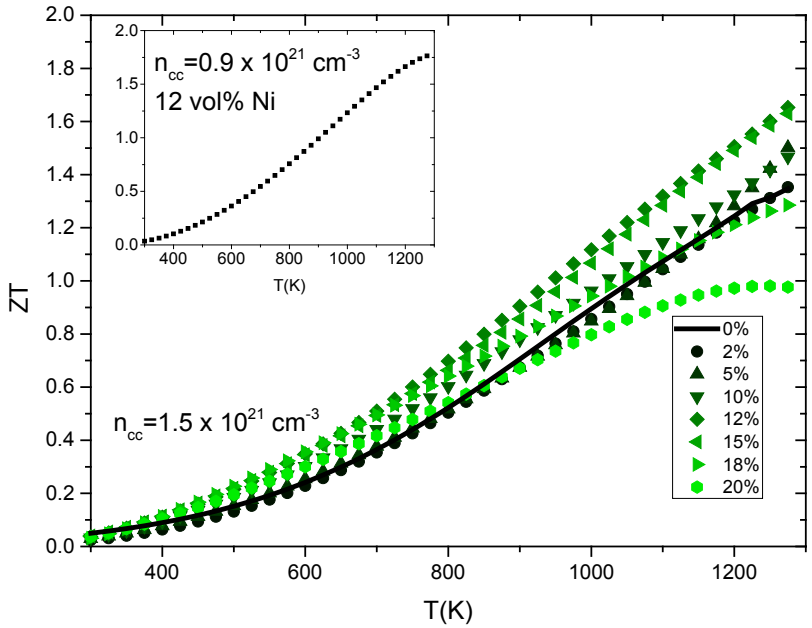

Figure 4.1 The thermoelectric figure of merit zT of $La_{3-x}Te_4$-Ni composites as a function of Ni vol%. The 12-15 vol% range improves the zT relative to $La_{3-x}Te_4$ containing no Ni. Lowering the carrier concentration of $La_{3-x}Te_4$ and creating a 12 vol% led to a high zT~1.8 @ 1275 K (inset).

Similar to the ordered geometries, the percolated Ni network is able to achieve a similar effect of improving upon the transport properties leading to higher power factors (see Fig. 4.2 and Fig. 4.3). Below the percolation threshold of 10 vol%, Ni has no effect upon the electrical and thermal transport properties. Evidence of percolation is observed only above 10 vol% Ni in the

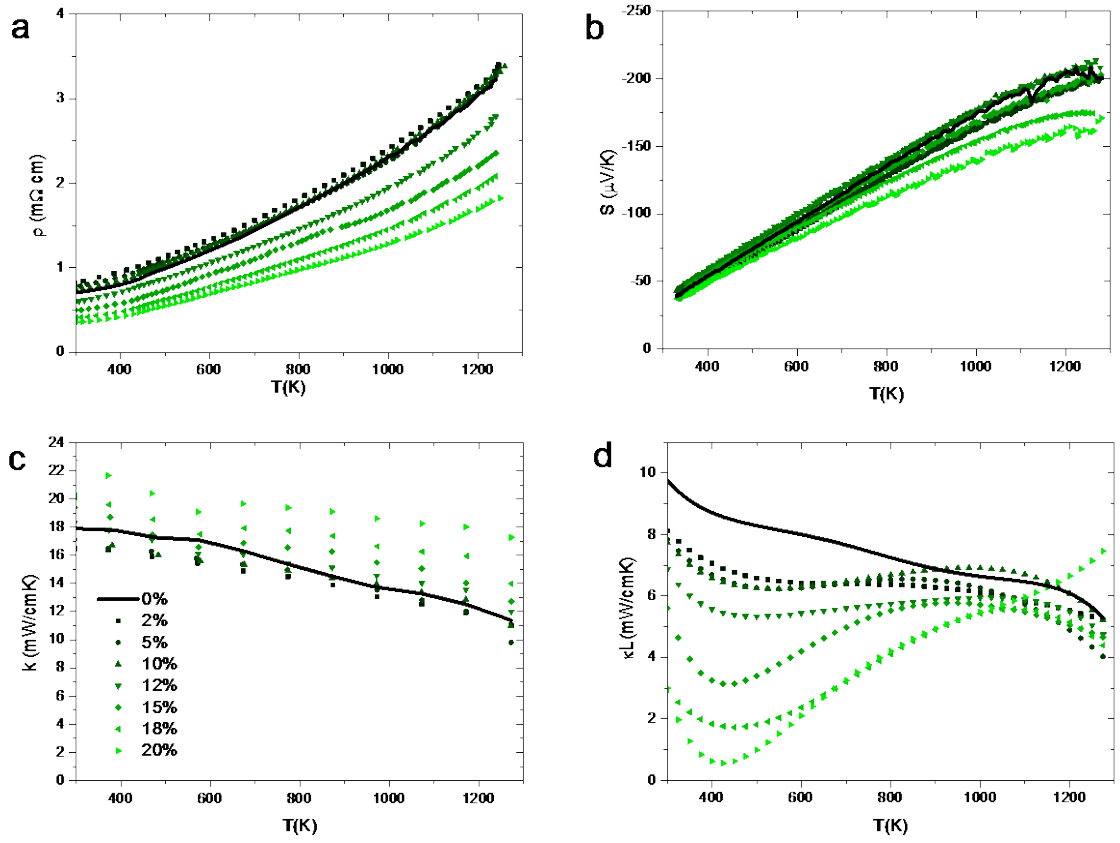

Figure 4.2 The high temperature electronic and thermal transport properties of $La_{3-x}Te_4$-Ni composite as a function of vol% Ni. a) The percolation threshold is reached at 12 vol% Ni and the electrical resistivity of the composite decreases with increasing Ni content. b) The Seebeck coefficient decreases beyond 15 vol% Ni. c) The thermal conductivity increases at greater than

15 vol% Ni. d) There is evidence of thermal scattering with increasing Ni content as reflected in the lower lattice thermal conductivity of the composites.

electrical resistivity; after which the resistivity decreases inversely proportional to the increasing Ni content (Fig. 4.2a). A greater connected Ni phase is also observed in the microstructure (Fig. 4.4). Interestingly, the reduction in electrical resistivity is not mirrored by an expected decrease in the Seebeck coefficient or increase in the thermal conductivity in the range of 12-15 vol% Ni (Fig. 4.3). At 18 vol% Ni and above, the metallic character of the Ni reduces the Seebeck coefficient and increases the thermal conductivity following the progression toward more metallic behavior. The end result is a loading range (of 12-15 vol%) where the electrical resistivity is decoupled from the other two transport properties resulting in an improved power factor and improved zT for the composite material.

Initially, $La_{3-x}Te_4$ was produced with a carrier concentration of 1.5 x 10^{21} cm^{-3} (Fig. 4.1) to match the previously determined optimum carrier concentration[8]. We utilized the decoupled transport properties and improved upon the Seebeck coefficient through reduction of the carrier concentration to 0.9 x 10^{21} cm^{-3}. As expected, the lower carrier concentration resulted in a higher starting electrical resistivity but incorporation of 12 vol% Ni reduced the resistivity of the composite. Coupled with the higher Seebeck coefficient of the base material, an improved overall zT = 1.8 @ 1273 K (Fig. 4.1 inset) was achieved.

4.5 Model for zT Improvement in Percolated $La_{3-x}Te_4$-Ni Composites

Although Fei and Bergman demonstrated that is it theoretically possible to improve upon the power factor in their simulated model system[7], they noted that zT is hampered by the high

thermal conductivity of the inert metal inclusion. However, the mechanism driving the improvement of zT for the percolated composites differs compared to their model system allowing for an increase in zT. First, a percolation threshold in which no change in transport properties up to 10 vol% is observed. This contrasts to their layered structures with smoothly

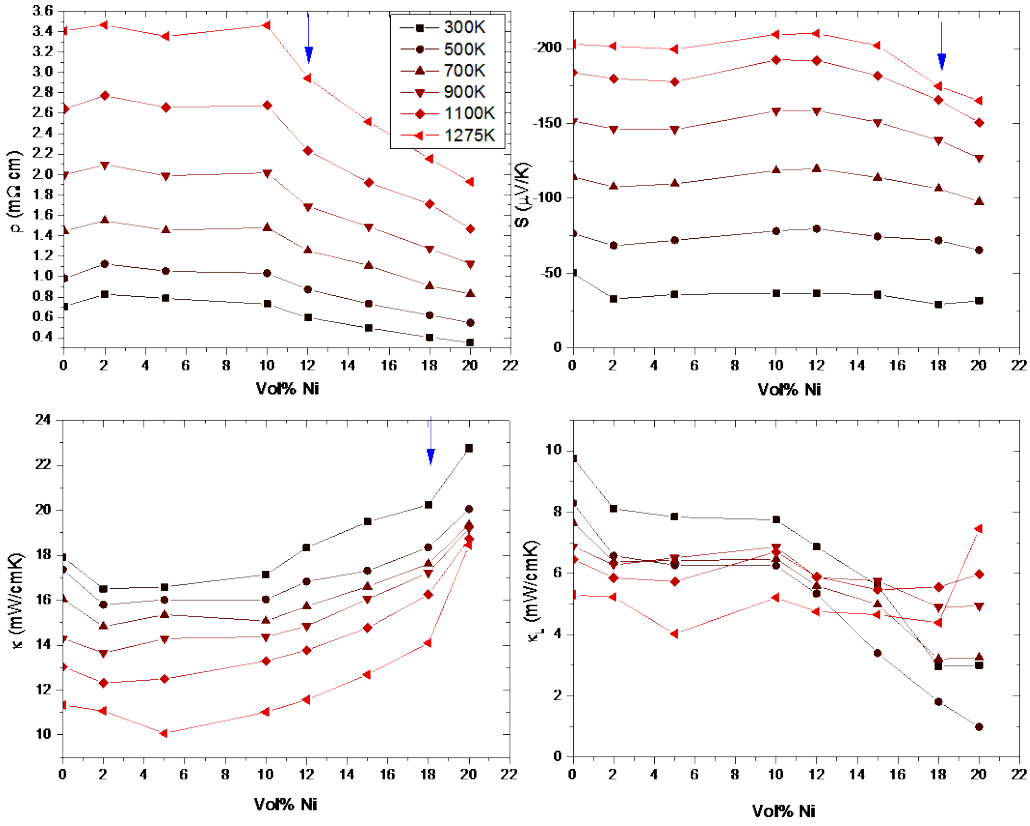

Figure 4.3 High temperature transport properties as a function of vol% Ni. a) The electrical resistivity decreases once the percolation limit is reached at 10 vol% Ni. b) The Seebeck coefficient decreases at 18 vol% Ni. c) The thermal conductivity increases at 18 vol%. d) The lattice thermal conductivity decreases as a function of increasing vol% except for 20 vol%.

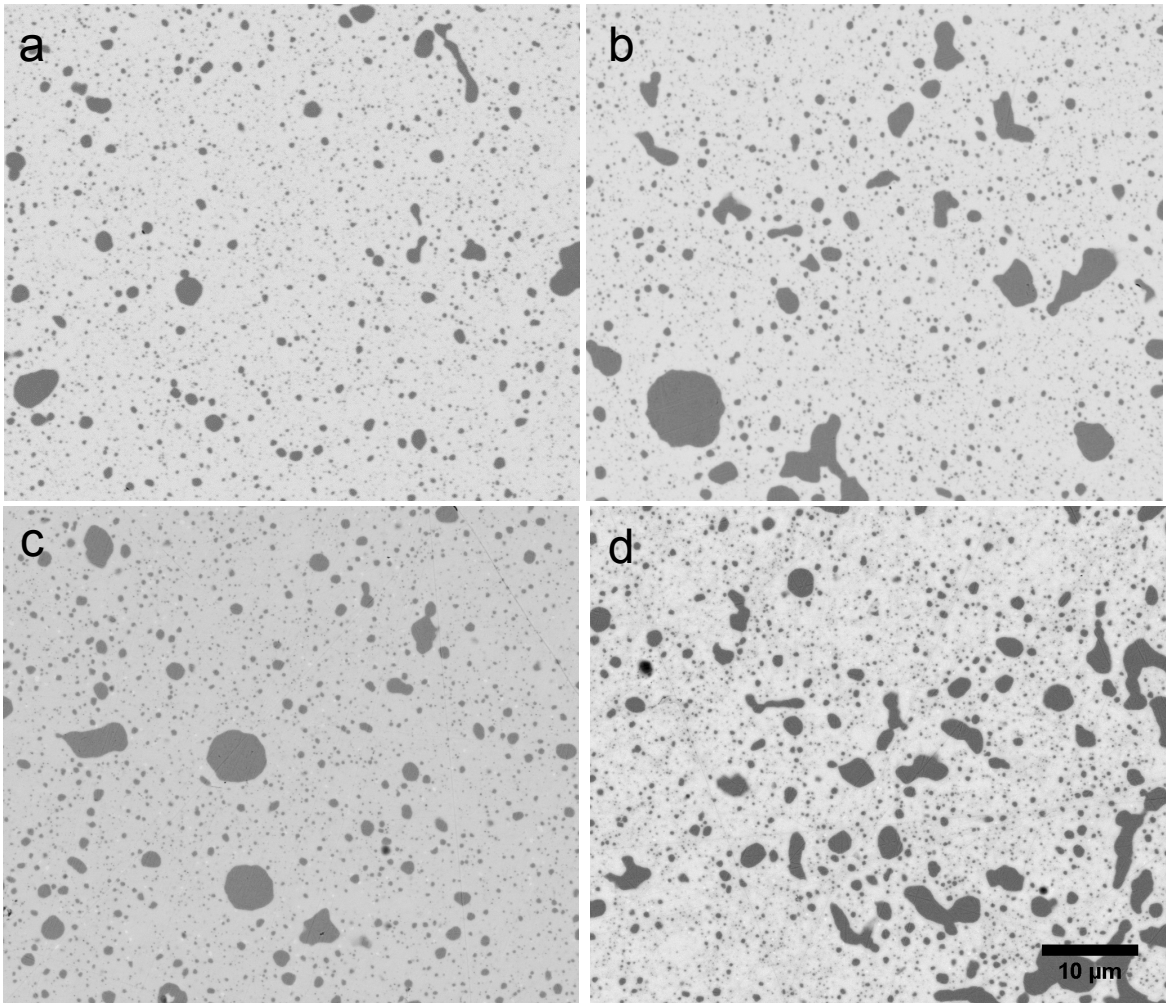

Figure 4.4 Backscattered electron scanning electron micrographs of the $La_{3-x}Te_4$-Ni composite. Increasing the vol% of Ni shows a greater degree of connectivity as the vol% of Ni increases: a)10 vol%; b) 12 vol%; c) 15 vol%; and d) 18 vol%.

varying properties punctuated with local minima and maxima. Furthermore, the percolated $La_{3-x}Te_4$-Ni composites exhibit a decoupling of the Seebeck and thermal conductivity from the electrical resistivity, allowing for an enhanced zT. The delayed reduction of the Seebeck coefficient can be understood as a combination of two effects. First, the high thermal conductivity of the Ni particles relative to $La_{3-x}Te_4$ results in regions where Ni can act as a

thermal shunt rendering it essentially as a void in terms of the Seebeck coefficient. It has been shown in other thermoelectric materials that the Seebeck coefficient is largely unaffected by voids[11]. This delays the effect of the lower Seebeck of Ni until beyond the percolation threshold. Second, the Seebeck reduction by Ni beyond the threshold of >15 vol% is observed, but is tempered by the relatively high Seebeck of the metal inclusions (Fig. 4.2b and 4.3). Pure Ni has an appreciable Seebeck coefficient of -35 μV/K at 1275 K[12], which is ~15% of the Seebeck of $La_{3-x}Te_4$ at that temperature and is of the same sign, which is important so that the two phases do not set up opposing electric fields[7]. This results in a moderated depression of the Seebeck coefficient once the percolation threshold is achieved. The effect of percolation on the Seebeck coefficient is in contrast to other thermoelectric composites that rely on the concept of energy

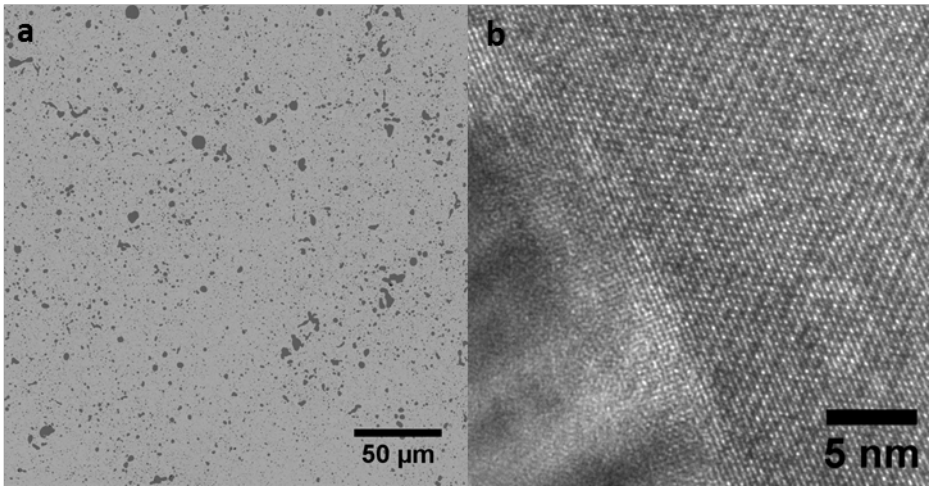

Figure 4.5 a) Backscattered electron (BSE)-SEM of a 12 vol% Ni $La_{3-x}Te_4$-Ni composite. The dark regions are Ni and light regions are $La_{3-x}Te_4$. Evidence for percolation is seen in the extended networks of Ni formed. **b)** High resolution transmission electron micrograph of the $La_{3-x}Te_4$-Ni composite interface. The lattice fringes of $La_{3-x}Te_4$ are visible on the right side of the image and there is no observable distortion to the fringes upon contact with the Ni particle on the left.

Filtering to raise the Seebeck coefficient [1,13]. The size of the Ni inclusions is in the micron regime (see Fig. 4.3, Fig 4.5 and Fig. 4.6) making energy filtering unlikely.

Critically, the increased power factor through reduction in resistivity occurs without an increase in the thermal conductivity in the 12-15 vol% window. This phenomenon would only be possible through phonon scattering. Utilizing the Wiedemann–Franz relation, it was calculated that there is a reduced lattice thermal conductivity proportional with increasing Ni content (Fig. 4.2d). Eventually beyond 15 vol%, the greater electronic contribution to thermal conductivity results in a higher total thermal conductivity producing a lower zT. Given the large size of the inclusions (Fig. 4.4, Fig. 4.5, and Fig. 4.6), it is unlikely that phonon scattering is occurring due to nano effects as suggested for other thermoelectric composite systems[2,14,15]. Therefore, the scattering is likely due to scattering at the interface between phases due to the large mismatch in thermal transport properties and possibly the formation of a thin interfacial reaction layer which contributes to scattering.

4.6 Chemical and Phase Analysis of $La_{3-x}Te_4$-Ni composites

To examine for the possibility of an interfacial reaction layer, compositional and phase characterization was carried out on the composite material. Powder X-ray diffraction of the consolidated materials indicates only Ni and $La_{3-x}Te_4$ phases (Fig. 4.7). Scanning electron microscopy (SEM) in backscattered electron (BSE) mode show that the boundaries between Ni particles and the $La_{3-x}Te_4$ phases are sharp and there is no observable reaction layer observed (Fig. 4.4, Fig. 4.5, and Fig. 4.6). Closer examination through high resolution transmission electron microscopy (HR-TEM) also indicates that the boundaries between the Ni and $La_{3-x}Te_4$ phases are abrupt down to the nanometer scale with no indication of reaction between the two

phases (Fig. 4.5b). Scanning tunneling electron microscopy (STEM) using energy dispersive spectroscopy (EDS) in conjunction with high angle annular dark field microscopy (HAADF)

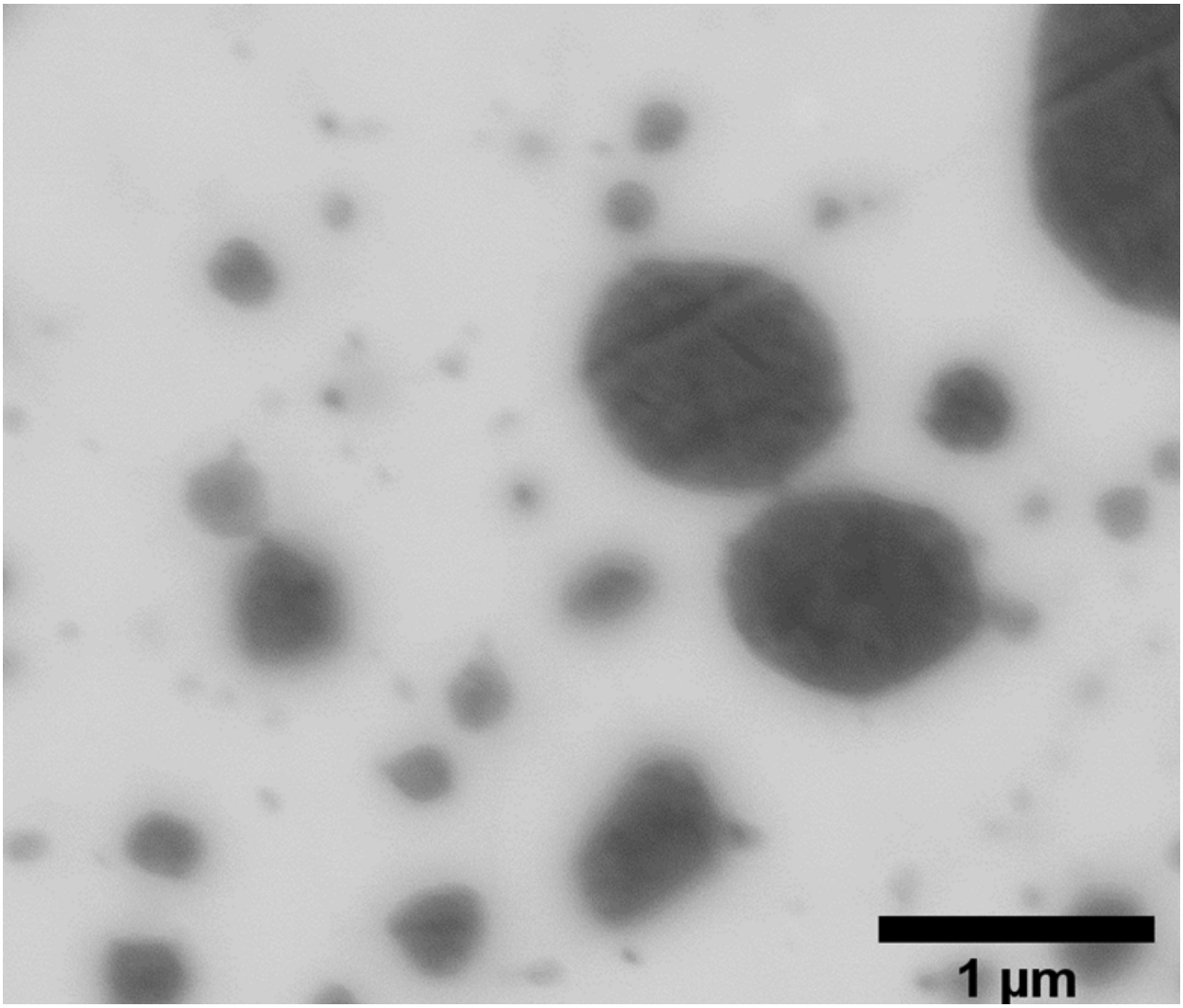

Figure 4.6 High magnification backscattered electron scanning electron micrograph of $La_{3-x}Te_4$-Ni composite. The interfaces between grains of the two $La_{3-x}Te_4$ and Ni are abrupt and suggest no reaction layer.

also suggests no reaction layer (Fig. 4.8 and Fig. 4.9). It has been reported through HR-TEM on single crystals of Bi_2Te_3 grown on GaAs, that interfacial layers can be atomically sharp with a reaction layer confined to 1 atomic plane[16]. The resolution necessary to examine for the possibility of a single atomic plane interface layer was not achievable for these polycrystalline samples. However, the reduced lattice thermal conductivity suggests the possibility of an interfacial layer between $La_{3-x}Te_4$ and Ni in conjunction with the mismatch of thermal transport properties between the two phases to be responsible for phonon scattering.

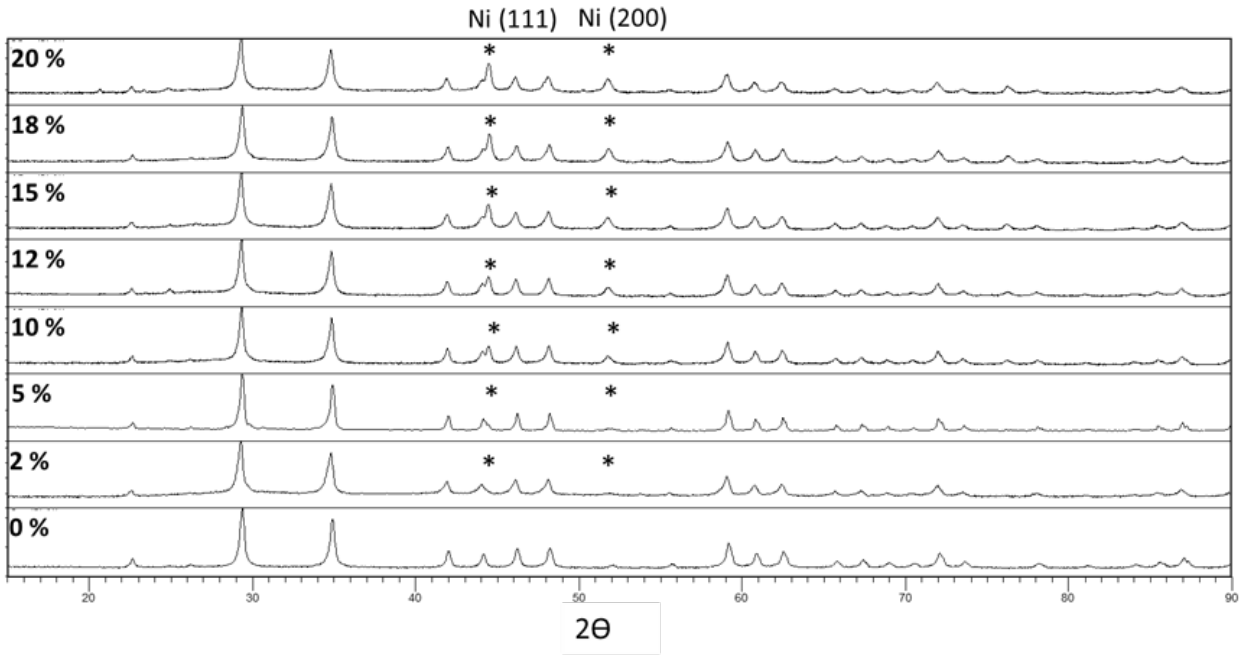

Figure 4.7 Powder X-ray diffraction spectra of $La_{3-x}Te_4$-Ni composites as a function of vol% Ni. Asterisks (*) highlight the Ni(111) and Ni (200) diffraction peaks. Only $La_{3-x}Te_4$ and Ni phases are present.

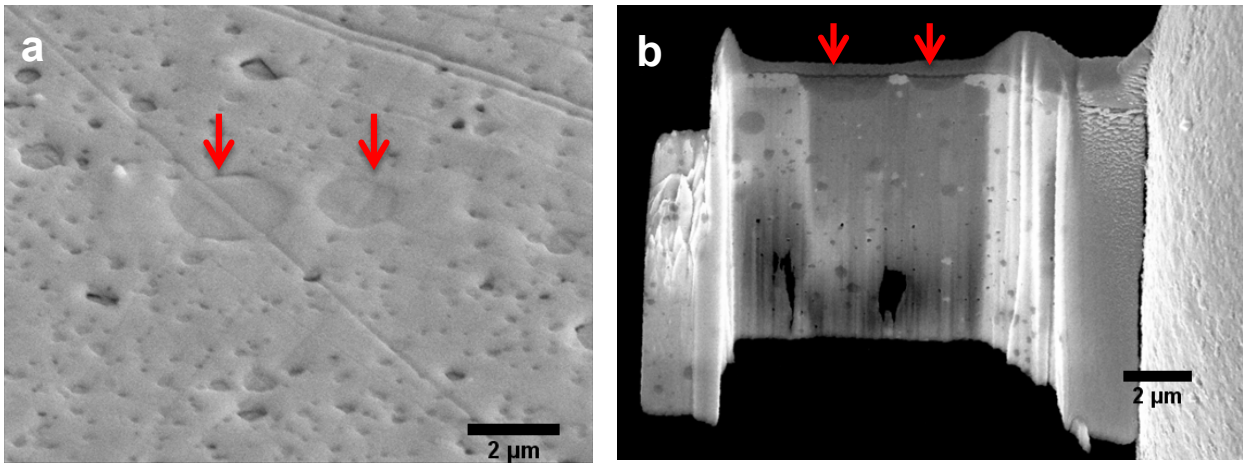

Figure 4.8 Focused ion beam preparation of transmission electron micrograph samples. a) Top view of the sample surface with Ni particles present on the surface indicated by the red arrows and b) Cross-section micrograph of the sample after thinning with a focused ion beam. The same surface Ni particles are indicated by the arrows.

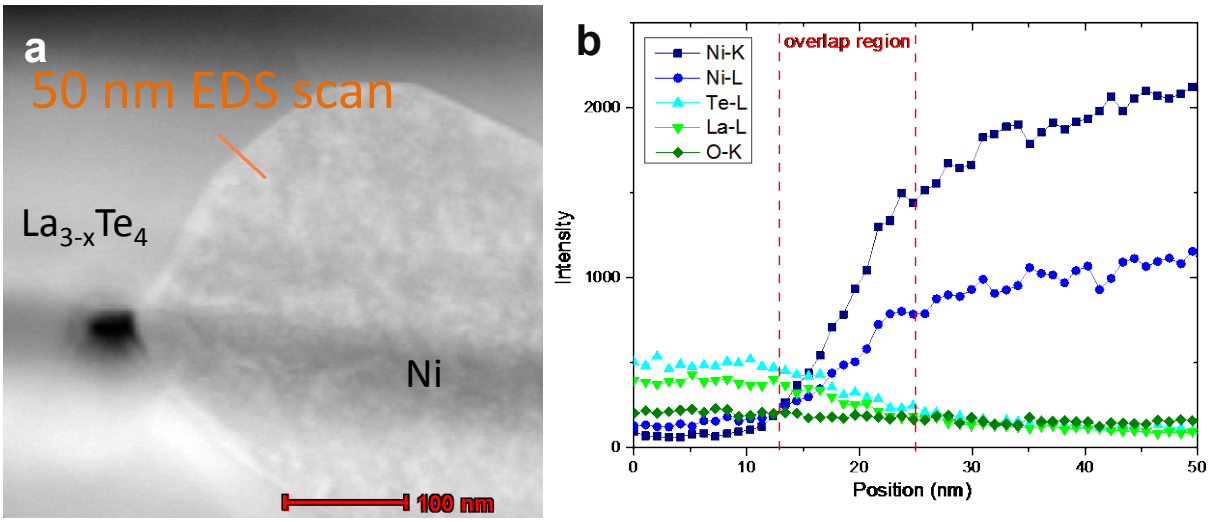

Figure 4.9 Scanning tunneling electron micrograph of the $La_{3-x}Te_4$-Ni interface. a) High angle annular dark field (HAADF) image of the interface. A 50 nm energy dispersive spectroscopy line scan is done across the grain boundary. b) There is an overlap region between the $La_{3-x}Te_4$ and Ni due to the round Ni particles. There is no indication of an oxide layer or secondary phase at the grain boundary.

The gradual transition of transport properties from $La_{3-x}Te_4$ to more Ni-like is in contrast to what has been observed in metal-insulator percolated composites where the transition is sharp[17,18]. It is not surprising that the transition is more complex as both $La_{3-x}Te_4$ and Ni phases are conductive. Computational modeling should be able to further clarify this effect and lead to a better understanding of the microstructure on transport properties.

4.7 Conclusions and Future Work

The $La_{3-x}Te_4$-Ni composites are of immediate interest to develop higher efficiency high temperature thermoelectrics and prototype device development is currently underway at the Jet Propulsion Laboratory. Perhaps more importantly, percolated composites with inert metal inclusions may prove as a viable means to improve upon other high zT thermoelectric materials across the whole temperature range. This inexpensive technique could drastically improve thermoelectric performance and enhance their use in terrestrial applications.

References

(1) Ko, D.-K.; Kang, Y.; Murray, C. B. *Nano Lett.* **2011**, *11*, 2841–2844.

(2) Biswas, K.; He, J.; Blum, I. D.; Wu, C.-I.; Hogan, T. P.; Seidman, D. N.; Dravid, V. P.; Kanatzidis, M. G. *Nature* **2012**, *489*, 414–418.

(3) Girard, S. N.; He, J.; Zhou, X.; Shoemaker, D.; Jaworski, C. M.; Uher, C.; Dravid, V. P.; Heremans, J. P.; Kanatzidis, M. G. *J. Am. Chem. Soc.* **2011**, *133*, 16588–16597.

(4) Hochbaum, A. I.; Chen, R.; Delgado, R. D.; Liang, W.; Garnett, E. C.; Najarian, M.; Majumdar, A.; Yang, P. *Nature* **2008**, *451*, 163–168.

(5) Boukai, A. I.; Bunimovich, Y.; Tahir-Kheli, J.; Yu, J.-K.; Goddard, W. a; Heath, J. R. *Nature* **2008**, *451*, 168–171.

(6) Bergman, D. J.; Levy, O. *J. Appl. Phys.* **1991**, *70*, 6821.

(7) Bergman, D. J.; Fel, L. G. *J. Appl. Phys.* **1999**, *85*, 8205–8216.

(8) May, A.; Fleurial, J.; Snyder, G. *Phys. Rev. B* **2008**, *78*, 1–12.

(9) Bux, S. K.; Blair, R. G.; Gogna, P. K.; Lee, H.; Chen, G.; Dresselhaus, M. S.; Kaner, R. B.; Fleurial, J.-P. *Adv. Funct. Mater.* **2009**, *19*, 1–8.

(10) May, A.; Singh, D.; Snyder, G. *Phys. Rev. B* **2009**, *79*, 1–4.

(11) Rowe, D. M. *J. Phys. D. Appl. Phys.* **1975**, *8*, 1092–1103.

(12) Bentley, R. E. *Handbook of Temperature Measurement Vol. 3: The Theory and Practice of Thermoelectric Thermometry*; 1998.

(13) Moizhes, B. Y.; Nemchinsky, V. A. In *Proc. for the 11th Int. Conf. on Thermoelectrics*; 1992.

(14) Yu, B.; Zebarjadi, M.; Wang, H.; Lukas, K.; Wang, H.; Wang, D.; Opeil, C.; Dresselhaus, M.; Chen, G.; Ren, Z. *Nano Lett.* **2012**, *12*, 2077–2082.

(15) Pei, Y.; Lensch-Falk, J.; Toberer, E. S.; Medlin, D. L.; Snyder, G. J. *Adv. Funct. Mater.* **2011**, *21*, 241–249.

(16) Houston Dycus, J.; White, R. M.; Pierce, J. M.; Venkatasubramanian, R.; LeBeau, J. M. *Appl. Phys. Lett.* **2013**, *102*, 081601.

(17) Aldrich, D. E.; Fan, Z. *Mater. Charact.* **2001**, *47*, 167–173.

(18) Clarke, D. R. *J. Am. Ceram. Soc.* **1992**, *75*, 739–758.

Chapter 5: Synthesis and Thermoelectric Properties of $La_{3-x}Ca_xTe_4$

5.1 Introduction

Thermoelectrics (TE) are solid state energy conversion devices which are able to generate power through the Seebeck effect or provide cooling through the Peltier effect. Thermoelectric generators (TEG) have consistently demonstrated their extraordinary reliability and longevity in support of the National Aeronautics Space Administration's (NASA) deep space science and exploration missions. The Voyager missions launched in 1977 utilize thermoelectric generators (TEGs) and are expected to continue to power the probe until 2025[1,2]. Most recently, NASA has used a TEG in the Curiosity Mars rover[3] with TEGs continuing to be a key technology for the future of deep space missions[4].

These proven state-of–practice "heritage" TE materials exhibit only modest thermal-to-electric energy conversion performance, resulting in relatively low system-level conversion efficiencies of 6 to 6.5%[5]. These heritage materials have been known since the late 1950's and 1960's, so that even the recently deployed multi-mission radioisotope thermoelectric generator (MMRTG) in the Curiosity rover builds upon 40-year old thermoelectric converter technology[6].

However, there is great potential for large gains in performance thanks to recent advances in materials synthesis, the discovery of novel compounds with complex crystal structures, and the ability to engineer with increasing precision micro- and nanostructured features. These factors, coupled with improved scientific understanding of electrical and thermal transport in such engineered materials, have potential for expanding the use of thermoelectric materials in space and terrestrial applications.

5.2 Theory

NASA's Radioisotope Power Systems Technology Advancement Program is pursuing the development of more efficient thermoelectric materials that can increase performance by a factor of two to four over state-of-practice systems. This is achieved through the synthesis of new materials with high zT and the enhancement of known thermoelectric materials through nanostructuring[7], dopant optimization[8], and emerging means to decouple the transport properties which govern efficiency[9,10]. The dimensionless thermoelectric figure of merit zT is defined as $zT = \frac{S^2}{\rho\kappa}T$ and directly impacts conversion efficiency. Good TE materials exhibit low thermal conductivity (κ), low electrical resistivity (ρ), and a large Seebeck coefficient (S). The thermal conductivity is the sum of its electronic contribution, κ_e, and its lattice contribution, κ_L.

The use of advanced materials, n-type and p-type filled skutterudites and rare earth compounds, has already resulted in doubling TE couple-level conversion efficiency up to 15% at the beginning of their life[6] which is over two times more efficient than the devices used in previous NASA missions. The high temperature (1273 K) n-type segment is lanthanum telluride, $La_{3-x}Te_4$, a self-doped refractory rare earth compound with a reported zT of 1.2 at 1273 K when x = 0.23 [11].

The compound, $La_{3-x}Te_4$, has a defect structure with the carrier concentration modified through controlling the lanthanum vacancy concentration. Material behavior can vary between metallic at x = 0 with one free e^- per formula unit (La_3Te_4) to an insulator at x = 0.33 with no free carriers (La_2Te_3). $La_{3-x}Te_4$ exhibits low thermal conductivity with glass-like κ_L values due to the complex crystal structure and scattering from the vacancies[12,13]. In addition, the material has

good electronic transport properties due to the favorable band structure of the material[12]. Near the optimum carrier concentration of n ~ 0.9 × 10^{20} cm^{-3}, conduction through light and heavy bands allows for efficient conduction of electrons while maintaining a high Seebeck coefficient.

From computational modeling, it has been found that the density of the states (DOS) in the conduction band is dominated by the lanthanum atoms[14]. Non-isoelectronic substitutions, such as Yb^{2+} on the La^{3+} site, was previously pursued as a means to modify the DOS, which could increase the Seebeck coefficient for this material[15]. In addition, the use of a divalent cation would allow for a finer control over the carrier concentration. The electronic local environment becomes $La_{3-x-y}^{3+}\blacksquare_{La,x}M_y^{2+}Te_4^{2-}e_{1-3x}^{1-}$, where $\blacksquare_{La,x}$ represents the number of vacancies in the system and M_y^{2+} represents the amount of non-isoelectronic metal substituents in the system. The theoretical carrier density can be calculated by $n = n_{max}(1 - 3x - y)$ where n_{max} = 4.5 × 10^{21} cm^{-3}, x is the vacancy ratio, and y is divalent cation ratio[15]. There is a threefold finer control of carrier concentration in the M^{2+} doped system compared to the vacancy-doped system. This makes it easier to synthesize samples with carrier concentrations in the optimized region of 0.8 × 10^{21} cm^{-3} to 1.2 × 10^{21} cm^{-3}, which had previously been difficult to obtain.[16] This doping also provides a way to create vacancy-free structures with identical carrier concentrations to the vacancy-doped samples, allowing for a separation of the impact on the lattice thermal conductivity of various defects on the La sublattice (vacancies, divalent atoms) versus electron-phonon interactions.

For this study, calcium was chosen as a dopant because of the definitive 2+ charge, similarity in size to La^{3+} which enhances the probability of successful substitution upon that site, and the difference in electronic properties from lanthanum atoms as it lacks electrons in the d

orbital. In this study, the calcium-doped compounds are vacancy-free to prevent conflation of the effects of calcium versus vacancies.

5.3 Experimental

Samples were prepared using powder metallurgy from the elements in an argon glove box as previously described.[17] The powders were then compacted in graphite dies through spark plasma sintering (SPS) under vacuum at temperatures above 1250 ºC and a pressure of 80 MPa yielding samples with >97% of theoretical density.

A Bruker D8 powder X-ray diffractometer using Cu Kα radiation was used to confirm phase purity and calculate the lattice parameter. A JEOL Super Probe electron microprobe analyzer and wave dispersive spectroscopy (WDS) was used to examine elemental compositions. The standards used for WDS were Te metal, $LaPO_4$, and $CaAl_2Si_2O_8$ (Anorthite), for the respective elements. The thermoelectric transport properties of the samples were measured using both custom setups and commercial instrumentation described elsewhere.[18,19]

5.4 Results

5.4.1 Characterization

The samples were analyzed for phase purity through powder X-ray diffraction. Powder X-ray diffraction was conducted on the polycrystalline material after sintering. A comparison of the X-ray diffraction patterns of $La_{3-x}Ca_yTe_4$ to the $La_{3-x}Te_4$ reference indicates that no second phases are present as seen in Figure 5.1. In addition, there is little change in the lattice parameter for the various calcium containing alloys. This is expected since the ionic radii of Ca^{2+} (114.0

pm) is similar in size to the ionic radii of La^{3+} (117.2 pm)[20] and there is little change in the lattice constant as a function of vacancy level.

The Ca^{2+} ions substitute for La^{3+} atoms and there is no observed evidence of calcium ordering as observed through the powder X-ray diffraction pattern (Figure 5.1)[21]. Additional single crystal X-ray diffraction would be necessary to definitively determine if there is any site preference for the calcium atoms. The vacancy limit for $La_{3-x}Te_4$ is x = 0.33, which results in a composition $La_{2.67}Te_4$. As shown in Figure 5.1, compositions below the threshold of $La_{2.67}$ are possible with substitutions by Ca. The solubility limit of calcium in the $La_{3-x}Te_4$ was not fully explored due to the limited thermoelectric usefulness of very low carrier concentration samples and the difficulty of handing samples in air, which increased with increasing calcium content. It was observed that oxygen and moisture sensitivity of the samples appeared to increase with increasing calcium content although both La and calcium are oxygen and moisture reactive metals.

The Ca-substituted samples were found to be homogeneous as seen through the electron microprobe backscattered electron (BSE) micrograph of a typical sample (Figure 5.2a). Wavelength dispersive spectroscopy (WDS) provided a way to quantitatively determine the stoichiometric amounts of each element. From the composition, the corresponding electron count was determined to calculate the carrier concentration. Comparison to the Hall carrier concentration as seen in Figure 2b indicates that the two results are in acceptable agreement with a slope m = 0.77, y-intercept b = 0.40, and $R^2 = 0.90$. Deviations from ideality can be attributed to the experimental limitations. Measurement of materials at high carrier concentrations resulted in low Hall voltages, thus decreasing the signal to noise ratio. For simplicity, the samples going forward will be referred to by the Hall carrier concentration x 10^{21} cm^{-3}.

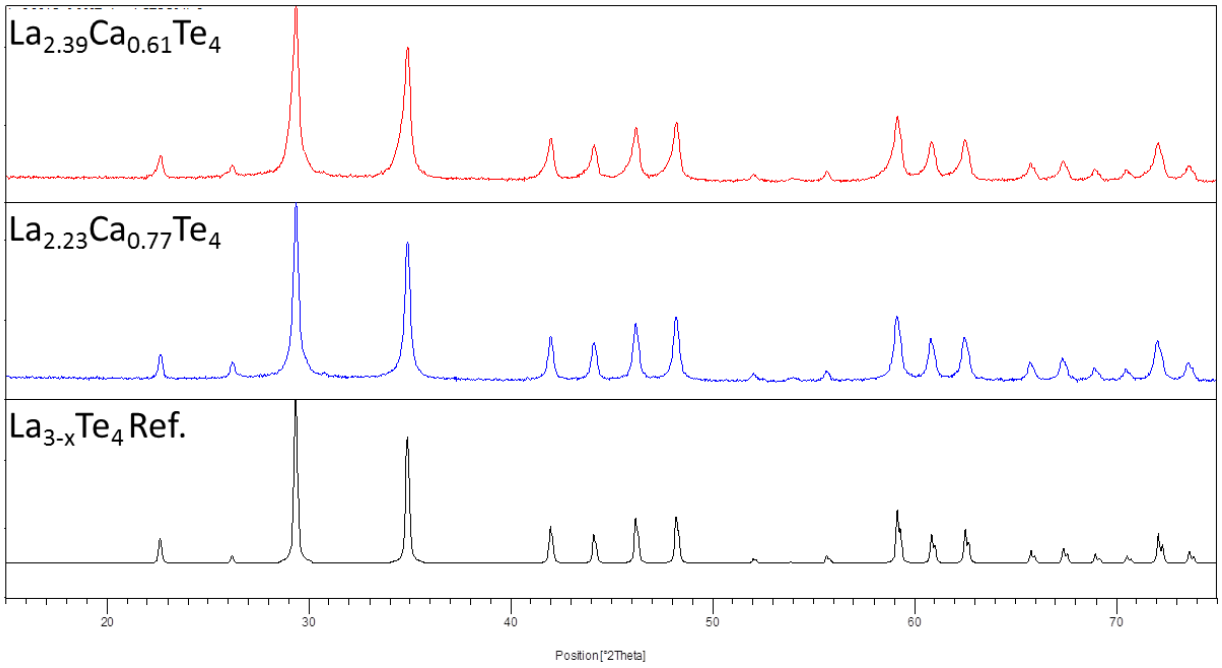

Figure 5.1 X-ray diffraction spectra of $La_{3-x}Ca_xTe_4$ compared to $La_{3-x}Te_4$ indicating that there are no secondary phases. In addition, there is no significant lattice expansion due to the similar size of the calcium atom to the La atom.

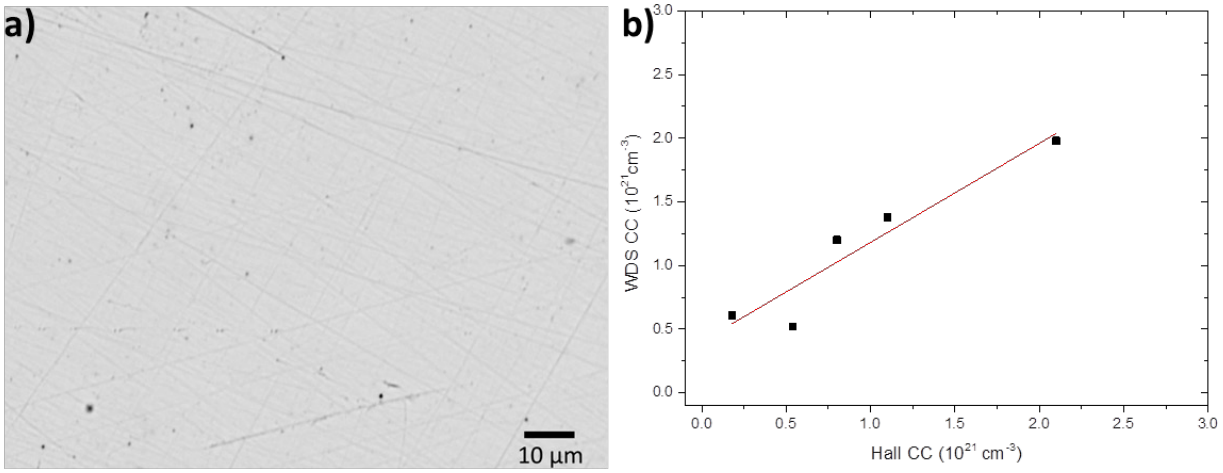

Figure 5.2 a) Backscattered electron scanning electron micrograph of a polished surface of $La_{2.23}Ca_{0.77}Te_4$ indicating that the sample is homogeneous. Minor porosity apparent as dark circles in the sample surface. **b)** There is good agreement between the calculated carrier

concentration, as dictated by the composition determined by wavelength dispersive spectroscopy (WDS), and the Hall carrier concentration.

5.4.2 Electronic Transport Properties

The temperature dependence of the electrical resistivity and Seebeck coefficient electrical resistivity are shown in Figures 5.3a and b, respectively for samples in a range of 0.2 x 10^{21} cm^{-3} to 2.1 x 10^{21} cm^{-3}. The electronic property measurements indicate degenerate heavily doped semiconductor behavior with increasing resistivity and magnitude of the Seebeck coefficient with temperature. The calcium doped samples follow similar trends to $La_{3-x}Te_4$ (dotted lines) and $La_{3-x}Yb_xTe_4$ (solid lines) for samples of comparable carrier concentrations previously reported by May *et al.* [8,11]. This is highlighted by the comparable resistivity and Seebeck curves of $La_{3-x}Ca_xTe_4$ at 2.1 x 10^{21} cm^{-3} compared to the $La_{3-x}Te_4$ and $La_{3-x}Yb_xTe_4$ samples at 1.6 x 10^{21} cm^{-3}. Although the Hall carrier concentration is measured to be higher, the samples exhibit higher electrical resistivity as well as higher Seebeck coefficient compared to the vacancy and ytterbium doped samples, which correspond with the samples having lower carrier concentration. The discrepancy is likely due to the limitation in measurement of carrier concentration.

The resulting electronic transport properties are in agreement with the results from X-ray diffraction and electron microprobe WDS in that the calcium atoms are substituting into the structure as an unambiguous +2 cation. Through calcium substitution, a finer control over carrier concentration is realized. The La^{3+}:Ca^{2+} composition can be adjusted to only add one electron at a time to the system, whereas the vacancy doped system adds three. This result reflects the initial hypothesis for enhanced control over carrier concentration as variations in carrier concentration progress more gradually as a function of stoichiometry. Fine carrier concentration

control is important for the $La_{3-x}Te_4$ system as near the optimized carrier concentration small deviations result in significant changes in the thermoelectric performance.

Furthermore, the result is noteworthy as the calcium atoms can successfully substitute lanthanum atoms seemingly without dramatic impact upon the electronic transport properties despite being very chemically different species.

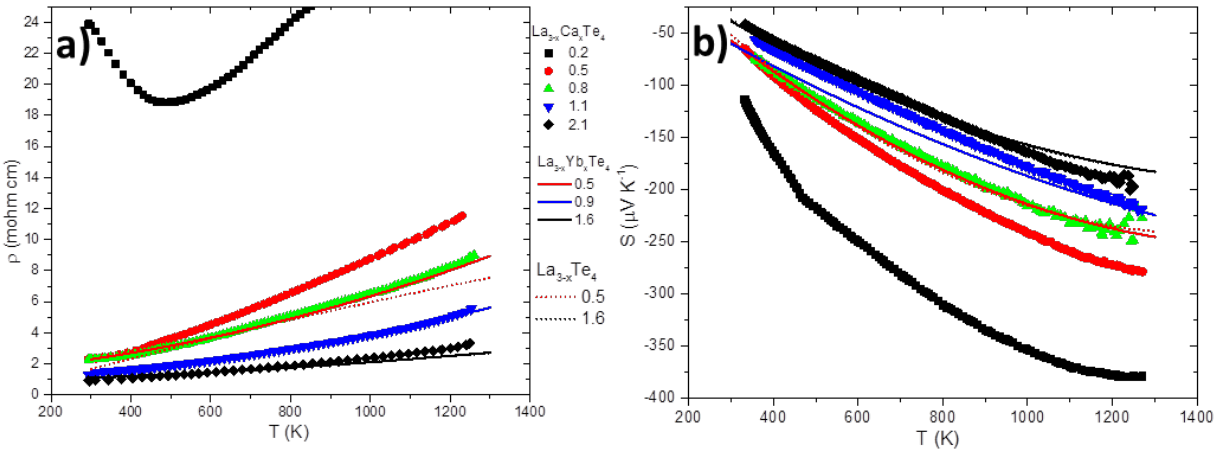

Figure 5.3 a) Electrical resistivity of $La_{3-x}Ca_xTe_4$ as a function of temperature. **b)** The Seebeck coefficient of $La_{3-x}Ca_xTe_4$ as a function of temperature. For comparison, the resistivity and Seebeck coefficient of $La_{3-x}Yb_xTe_4$[8] (solid lines) and $La_{3-x}Te_4$[11] (dotted lines) are plotted as well.

5.4.2 Thermal Transport Properties

The thermal conductivity and lattice thermal conductivity of $La_{3-x}Ca_xTe_4$ are shown in Figures 5.4a and Figure 5.4b, respectively. Thermal conductivity was calculated using measured thermal diffusivity, heat capacity, and thermal expansion from previously published differential scanning calorimetry results adjusted for calcium content using the Dulong-Petit law[13]. The total thermal conductivity is the sum of the lattice and electronic thermal conductivity $\kappa_t = \kappa_e + \kappa_l$.

To determine the lattice thermal conductivity, the electronic contribution to the total thermal conductivity was first calculated using the Wiedemann-Franz law $\kappa_e = \sigma LT$ where σ is the electrical conductivity, L is the Lorenz number, and T is the absolute temperature, followed by subtracting from κ_t. The Lorenz number is estimated assuming only acoustic phonon scattering and an estimation of the chemical potential from the Seebeck coefficient values as a function of temperature. The lattice thermal conductivity takes into account the bipolar contribution to thermal conductivity from thermally activated minority carriers which effect can be observed as a rise in the lattice thermal conductivity at high temperature. However, in the case of $La_{3-x}Ca_xTe_4$, $La_{3-x}Te_4$, and $La_{3-x}Yb_xTe_4$ near the previously optimized carrier concentration, the Fermi level is in the conduction band away from the conduction band edge and the material has a sufficient band gap, thereby limiting the effect of minority carriers.

The minimum lattice thermal conductivity is achieved at a carrier concentration of around 1.1×10^{21} cm^{-3} for the calcium-doped system. It is comparable to the lattice thermal conductivity for $La_{3-x}Te_4$ at a carrier concentration of 0.5×10^{21} cm^{-3}. It was previously noted that vacancies could be thought of as ideal point defects[11,13]. However, it has been shown here that calcium atoms can also lead to significant phonon scattering through a combination of point defect and ionized impurity scattering. The net effect of calcium substitution versus vacancies or ytterbium substitution upon the thermal conductivity is marginal.

A more comprehensive set of calcium-substituted samples, with and without lanthanum vacancies needs to be studied to be able to precisely ascertain the relative impact of lanthanum vacancies. The limits upon the scope of the experiments here show that the calcium atoms can also be utilized to limit the thermal conductivity.

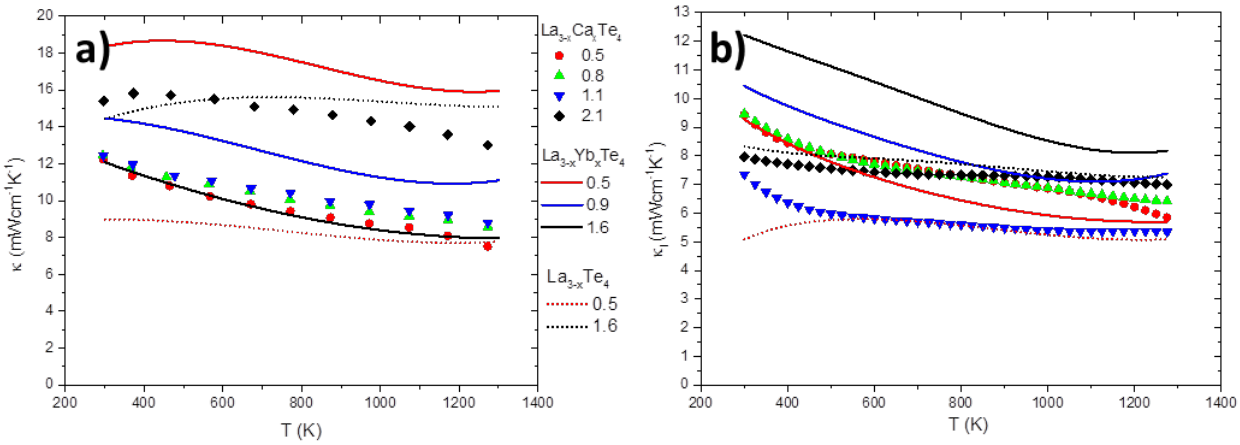

Figure 5.4 a) Total thermal conductivity of $La_{3-x}Ca_xTe_4$ as a function of temperature. **b)** The lattice thermal conductivity of $La_{3-x}Ca_xTe_4$ as a function of temperature. For comparison, the total thermal conductivity and lattice thermal conductivity $La_{3-x}Yb_xTe_4$[8] (solid lines) and $La_{3-x}Te_4$[11] (dotted lines) are plotted as well.

5.4.2 The Effect of Calcium Substitution Upon the Thermoelectric Figure of Merit

One of the major motivations for calcium substitution into the $La_{3-x}Te_4$ structure is to modify the density of states for the compound. It can be understood on a basic level that since the lanthanum atoms serve as the cations and the conduction electrons come from the lanthanum atoms, therefore the density of states of the conduction band will be controlled by the lanthanum atoms. The strong contribution of the lanthanum atoms to the conduction band has been verified through calculations[12]. Therefore, substitution by a drastically chemically different species such as calcium with no d electrons, would result in a different band structure possibly increasing the Seebeck coefficient. Calcium's contribution to the Seebeck effect can be analyzed through a Seebeck coefficient versus carrier concentration plot, often referred to as a Pisarenko plot, as shown in Figure 5.5a. The $La_{3-x}Ca_xTe_4$ data represented as the blue triangles are a close match

compared to the multiple parabolic band model, represented as the line, proposed by May *et al.*[12] There may be a marginally higher Seebeck coefficient in comparison to the model, but is likely within the noise of measurement of the Seebeck coefficient and/or the Hall carrier concentration. Therefore, there is likely no change in the band structure within the region of interest with substitution by Ca.

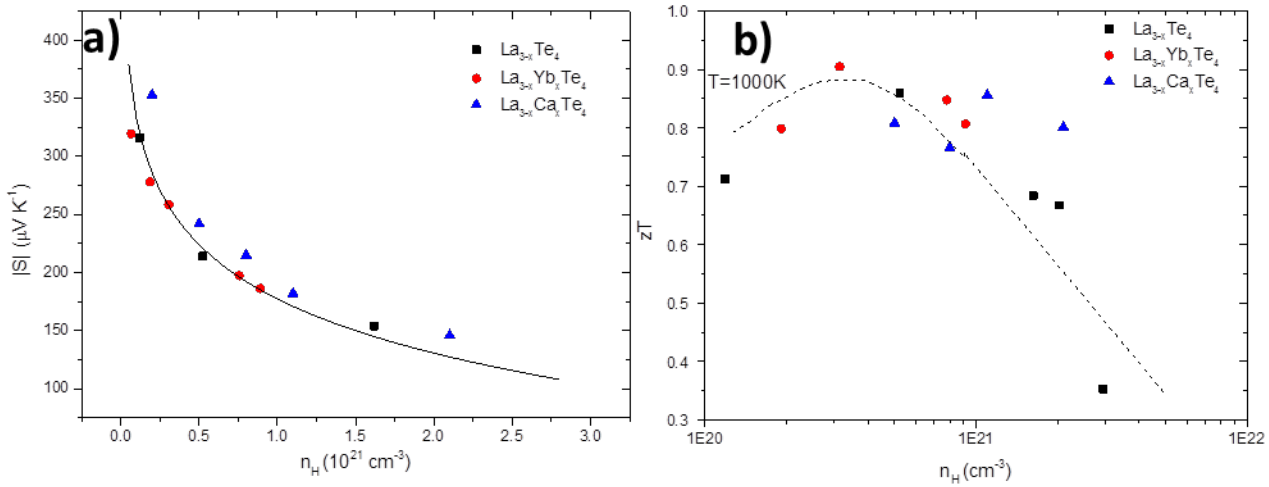

Figure 5.5 a) The absolute value of the Seebeck coefficient as a function of carrier concentration. **b)** The thermoelectric figure of merit zT as a function of carrier concentration at 1000 K. The results of the $La_{3-x}Ca_xTe_4$ match well to the previously calculated multiple parabolic band model (fit line) for $La_{3-x}Te_4$[12].

This result is reflected as well in the optimization of zT as a function of carrier concentration as can be seen in Figure 5.5b. The calcium doped samples fit moderately well for results with carrier concentrations less than 1 x 10^{21} cm^{-3}. The zT appears to remain higher at higher carrier concentrations and can possibly be explained by the uncertainty in the measurements of carrier concentration at high values. As suggested earlier in the electrical resistivity and Seebeck coefficient measurements presented in Figure 5.3, there is likely an

overestimation of the Hall carrier concentration. This correction for the overestimation would shift the curve to the points closer to the model curve proposed by May *et al.*[12]

The similarity of the calcium doping to ytterbium doping and vacancy doping is apparent in the zT plot as a function of temperature as shown in Figure 5.6. A peak zT ~ 1.2 at 1273 K was measured at a carrier concentration 1.1 x 10^{21} cm^{-3}, which is comparable to the peak zT reported by for $La_{3-x}Te_4$[11] and $La_{3-x}Yb_xTe_4$[8].

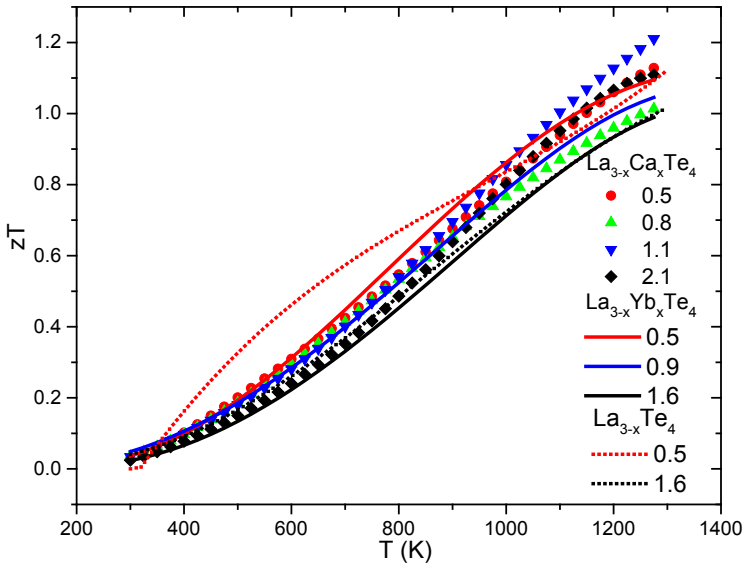

Figure 5.6 The thermoelectric figure of merit zT as a function of temperature for $La_{3-x}Ca_xTe_4$ as a function of temperature. The peak zT at 1273 K is ~1.2 and is comparable to results for $La_{3-x}Yb_xTe_4$[8] and $La_{3-x}Te_4$[11].

5.5 Preliminary Computation Modeling

The effect of calcium doping upon the conduction band is being studied through computational modeling. The calculations are still in progress at the Jet Propulsion Laboratory by Trinh Vo and Paul von Allmen and preliminary calculations for the density of states are shown in Figure 5.7 for several carrier concentrations.

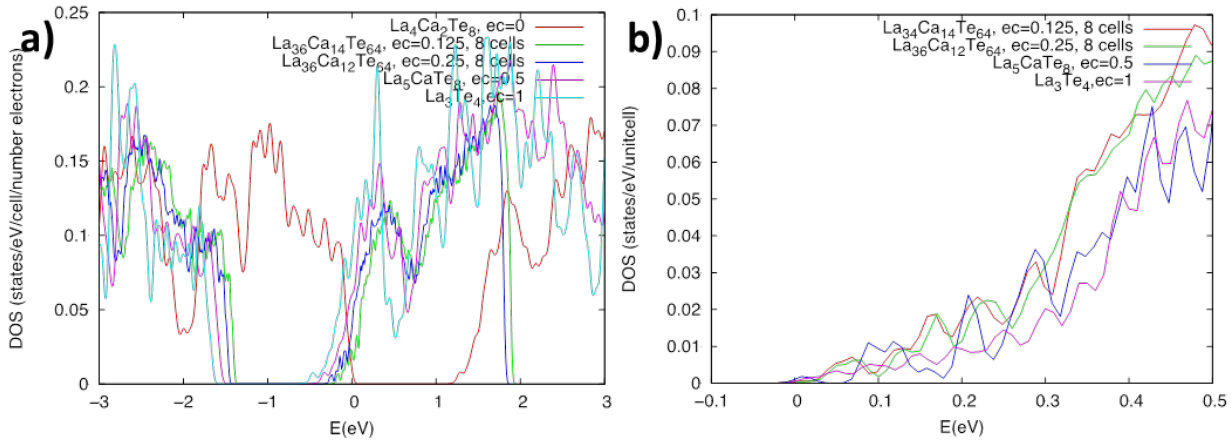

Figure 5.7 a) The calculated density of states for $La_{3-x}Ca_xTe_4$ at various carrier concentrations and for La_3Te_4**. b)** An examination of a narrower energy window of the conduction band for the various cases. The band edges have been offset to provide a common starting point to allow for comparison.

The calculated density of states for $La_{3-x}Ca_xTe_4$ for several carrier concentrations and for the fully filled La_3Te_4 is shown in Figure 5.7a. A higher resolution examination of a narrow energy window of the conduction band emphasizes the region of interest near the conduction band edge in Figure 5.7b. In addition, the conduction bands have been offset to a common zero point to allow for better comparison of the band features. Two features stand out for cases with calcium substitution. First, there is a small change in the slope and magnitude of the density of states at E = 0.23 eV. Second, there is a much larger magnitude and change in the slope of the density of states occurring at E ~ 0.35 eV. The higher energy change to the band structure is likely too high to be accessed even at 1300 K and therefore the feature at E = 0.23 eV was investigated. It has been calculated that at 1200 K, $La_{2.125}Ca_{0.875}Te_4$ ($La_{34}Ca_{14}Te_{64}$) would need to have a carrier concentration of 9.45 x 10^{21} cm^{-3} to occupy states at this energy level. However, based on electron counting rules of La^{3+} and Ca^{2+}, such a composition would only have a carrier

concentration of 0.56 x 10^{21} cm^{-3}. It is therefore impossible to even reach this lower energy feature with just calcium substitution.

The situation is even worse for compounds with lower calcium content. For $La_{2.25}Ca_{0.75}Te_4$ ($La_{36}Ca_{12}Te_{64}$), the carrier concentration would need to be 2.9 x 10^{21} cm^{-3} at 1200 K. This carrier concentration is greater than the structural limit of n_{max} 4.5 x 10^{21} cm^{-3} for La_3Te_4. Preliminary calculations seem to indicate that the modification to the density of states of the conduction band is possible through calcium substitution, but it is occurring at too high of an energy. This result would explain the experimentally observed lack of change in the Seebeck coefficient from calcium doping.

Ongoing work is going to calculate the Seebeck coefficient of these compositions and will likely confirm the experimental results of the lack of change in the Seebeck coefficient. These preliminary results suggest that the calcium substitutions are having an effect on the density of states, but they would require higher carrier concentrations than possible with just Ca^{2+} substitutions. A possibility would be X^{-1} halide substitution on the Te^{2-} with a composition high in calcium. This would allow for an increased carrier concentration at calcium compositions where the position of the density of states feature shifts to lower energies.

5.6 Conclusions

The successful doping of $La_{3-x}Te_4$ with Ca^{2+} was achieved through powder metallurgy and indicates that substitutions of Ca^{2+} for La^{3+} is possible for a wide range of carrier concentrations. General behavior of the material is similar to that of La-vacancy controlled doping of $La_{3-x}Te_4$ first described by May *et al*[16]. Finer control over carrier concentration is achieved by having a divalent cation substituted system rather than a La vacancy-doped system. Additionally, the

definitive oxidation state of Ca^{2+} eliminates any ambiguity introduced from doping with mixed valent Yb^{2+}/Yb^{3+}[8]. Early computation modeling results suggest that there is a modification to the density of state of the conduction band through calcium doping. However, the modifications occur at too high of an energy level to affect the Seebeck coefficient at achievable carrier concentrations with just calcium doping.

REFERENCES

1. Voyager: Spacecraft Lifetime. Accessed: January 17. 2014. Updated: September 10, 2013. http://voyager.jpl.nasa.gov/spacecraft/spacecraftlife.html2013.

2. R. D. Abelson, in *CRC Handbook on Thermoelectrics*, ed. D. M. Rowe, CRC Press, 2006.

3. *Multi-Mission Radioisotope Thermoelectric Generator (MMRTG)*, 2013.

4. G. Schmidt, L. Dudzinski, and T. Sutliff, in *Radioisotopes - Applications in Physical Sciences*, ed. N. Singh, American Institute of Aeronautics and Astronautics, Reston, Virigina, 2011.

5. *Space Radioisotope Power Systems: Multi-Mission Radioisotope Thermoelectric Generator*, 2008.

6. S. Bux, J.-P. Fleurial, T. Caillat, B. Y. Li, K. Star, S. Firdosy, V. Ravi, C.-K. Huang, B. Cheng, P. Gogna, J. M. Ma, P. von Allmen, and T. Vo, *11th Int. Energy Convers. Eng. Conf.*, 2013.

7. S. K. Bux, J. P. Fleurial, R. Blair, P. Gogna, T. Caillat, and R. B. Kaner, in *Materials Research Society Symposium Proceedings*, 2009, vol. 1166.

8. A. F. May, J.-P. Fleurial, and G. J. Snyder, *Chem. Mater.*, 2010, **22**, 2995–2999.

9. M. S. Dresselhaus, G. Chen, Z. F. Ren, J.-P. Fleurial, P. Gogna, M. Tang, D. Vashaee, H. Lee, X. Wang, G. Joshi, G. Zhu, D. Wang, R. Blair, S. Bux, and R. Kaner, in *Materials Research Society Symposium Proceedings*, 2008, vol. 1044.

10. D.-K. Ko, Y. Kang, and C. B. Murray, *Nano Lett.*, 2011, **11**, 2841–2844.

11. A. May, J. Fleurial, and G. Snyder, *Phys. Rev. B*, 2008, **78**, 1–12.

12. A. May, D. Singh, and G. Snyder, *Phys. Rev. B*, 2009, **79**, 1–4.

13. O. Delaire, A. F. May, M. A. Mcguire, W. D. Porter, M. S. Lucas, M. B. Stone, D. L. Abernathy, V. A. Ravi, S. A. Firdosy, and G. J. Snyder, *Phys. Rev. B*, 2009, **80**, 1–9.

14. A. May, D. Singh, and G. Snyder, *Phys. Rev. B*, 2009, **79**, 1–4.

15. A. F. May, J.-P. Fleurial, and G. J. Snyder, *Chem. Mater.*, 2010, **22**, 2995–2999.

16. A. May, J.-P. Fleurial, and G. Snyder, *Phys. Rev. B*, 2008, **78**, 1–12.

17. A. May, J. Snyder, J.-P. Fleurial, and M. S. El-Genk, *AIP Conf. Proc.*, 2008, **969**, 672–678.

18. J. A. Mccormack and J. Fleurial, *Mater. Res. Soc. Symp. Proc.*, 1991, **234**, 135–143.

19. C. Wood, D. Zoltan, and G. Stapfer, 1985, **56**, 719–722.

20. R. D. Shannon, *Acta Cryst.*, 1976, **A32**, 751–767.

21. F. L. Carter, *J. Solid State Chem.*, 1972, **5**, 300–313.

Chapter 6: Future Work

6.1 Developing Prototype $La_{3-x}Te_4$-Ni Composite Thermoelectric Devices

Development is now underway at the Jet Propulsion Laboratory to produce functional prototype devices with $La_{3-x}Te_4$-Ni composites and verify the improved thermoelectric performance at the device level. In this materials system, it has been demonstrated that the zT is almost a two-fold improvement over the legacy material $Si_{1-x}Ge_x$[1], which could have significant implications for new high efficiency thermoelectric couples. These thermoelectric efficiency results need to be validated because of the complexity of measuring the three interdependent properties that comprise the thermoelectric figure of merit zT, which can make zT values subject to errors. In the work reported in this thesis, an intensive effort was made to ensure that the results are reproducible and done on single samples/batches of material to remove the pitfalls of sample inhomogeneity. Corroboration of the materials properties at the device level is the critical next step toward maturation of the technology.

Furthermore, many thermoelectric materials fail to meet the stringent requirements for space applications. The high value of space missions and strenuous operating conditions require very high reliabilities over long mission durations. In this respect, $Si_{1-x}Ge_x$ has been a remarkable thermoelectric material because it has been in continuous operation since 1976 with a hot side temperature of 1270 K, a large temperature differential of 714 K, and exposure to radiation from space[2]. Materials such as $CuSe_2$ have shown promise in the early research stages for incorporation into thermoelectric devices, but were unable to withstand the rigors of space travel[3]. Some efforts have already shown $La_{3-x}Te_4$ to be a promising new candidate for the next

generation of radioisotope thermoelectric generators[4]; likewise, these same studies need to be conducted on the new composite materials.

6.2 Developing New Percolated Composites

The discovery of high zT percolated $La_{3-x}Te_4$-Ni composites has been a serendipitous discovery in the field of thermoelectrics. Thermoelectric-metal composites can be the basis for substantial zT improvements for materials across a wide variety of temperature ranges. The proposed mechanism for the improvement in zT in the $La_{3-x}Te_4$-Ni composites is the low resistivity percolated Ni network which allows for a reduction in electrical resistivity while maintaining a similar Seebeck coefficient and thermal transport properties. Based on the studies so far, it appears as though such a mechanism is not unique and should be suitable for improving other thermoelectric materials.

Improvements in the Skutterudite $CoSb_3$ class of thermoelectric materials would be of the greatest commercial interest. The peak efficiency of $CoSb_3$ is achieved at a lower temperature range making it suitable for many waste heat recovery applications[5]. However, each new material system requires a series of screening studies to identify potential inclusion particles which are chemically compatible with the material. It will likely be more challenging for Skutterudites as there are often multiple dopant elements which increase the chances for reactivity with a secondary phase. Furthermore, there are atoms which reside in interstitial sites crucial for optimization of thermoelectric properties which are loosely bound in the $CoSb_3$ structure making them more likely to be reactive with secondary phase particles. Nevertheless, this is a high priority goal as an improvement in this material would have a substantial impact in

the field of thermoelectrics toward commercial applications and would further validate the percolation model to improve zT.

6.3 Synthesis and Doping Studies of $La_{3-x}M_xTe_{4-y}Q_y$

The initial study into $La_{3-x}Ca_xTe_4$ did not yield a significantly improved zT as originally hypothesized, but it has provided important insights into the robust chemistry available to $La_{3-x}Te_4$. For example, doping on the La site can modify the density of states of the conduction band to improve the Seebeck coefficient. It has been previously shown that the $La_{3-x}Te_4$ system is conducive to doping both on the rare earth site and the chalcogenide position. On the rare earth position, cation doping is possible with rare earths or alkali metals. While May et al. initially conducted experiments with Yb, other +2 rare earths such as Sm and Eu can potentially be substituted into the structure[6]. Overall it is still not understood the extent possible for doping of the structure. It has been demonstrated through the percolated composite work that certain elements such as Ni and Fe do not appear to substitute into the La position in any appreciable amount. However, it may be possible to dope with other transition metals or alkali metals onto the La position providing further manipulation of the conduction band and carrier concentration. The chemical phase space for $La_{3-x}Te_4$ is large and will continue to be an interesting platform for further research.

In addition, continued work is needed to improve $La_{3-x}Ca_xTe_4$. With just Ca, the modifications to the density of states of the conduction band are at too high of an energy to affect the Seebeck coefficient. However, this provides exciting opportunities for the future development of multiply doped $La_{3-x}M_xTe_{4-y}Q_y$. Computational modeling suggests that at higher Ca concentrations, the increase in the density of states occurs just beyond the Fermi level.

Substitution of a halide into the chalcogenide position in the structure could raise the Fermi level while primarily affecting only the density of states of the valence band. This could lead to increase in the Seebeck coefficient while controlling the carrier concentration on both the rare earth and chalcogenide positions.

Some initial work has been done with Ba substitutions into $La_{3-x}Te_4$, but it has been challenging to reproduce the results. The $La_{3-x}Ba_xTe_4$ compounds were very air sensitive and it was difficult to source a high purity oxide free Ba ingot. As observed in Fig. 6.1, an oxide peak is present in the XRD for some $La_{3-x}Ba_xTe_4$ samples despite being produced under identical conditions. A possible explanation could be Ba ingot inhomogeneity and efforts to purify Ba metal from BaO through vapor transport prior to synthesis could improve control of the oxygen content. It is interesting to note that there is an observed lattice expansion in $La_{3-x}Ba_xTe_4$ which is expected due to the larger size of Ba. This will likely have an effect on the density of states and band structure of the conduction band perhaps improving the Seebeck coefficient. Initial results have been promising, but inconclusive, due to the difficulty in reproducing compounds because of the oxide content.

Finally, it was beyond the initial scope of this work to produce $La_{3-x}Te_4$ with a mixture of dopants and vacancies. It has been shown in the past that vacancies were not only an important means of controlling carrier concentration; the vacancies are also in part responsible for phonon scattering and the low thermal conductivity in $La_{3-x}Te_4$[7]. Therefore, it is likely that a mixture of vacancies and dopants will yield the most favorable properties for $La_{3-x}Te_4$.

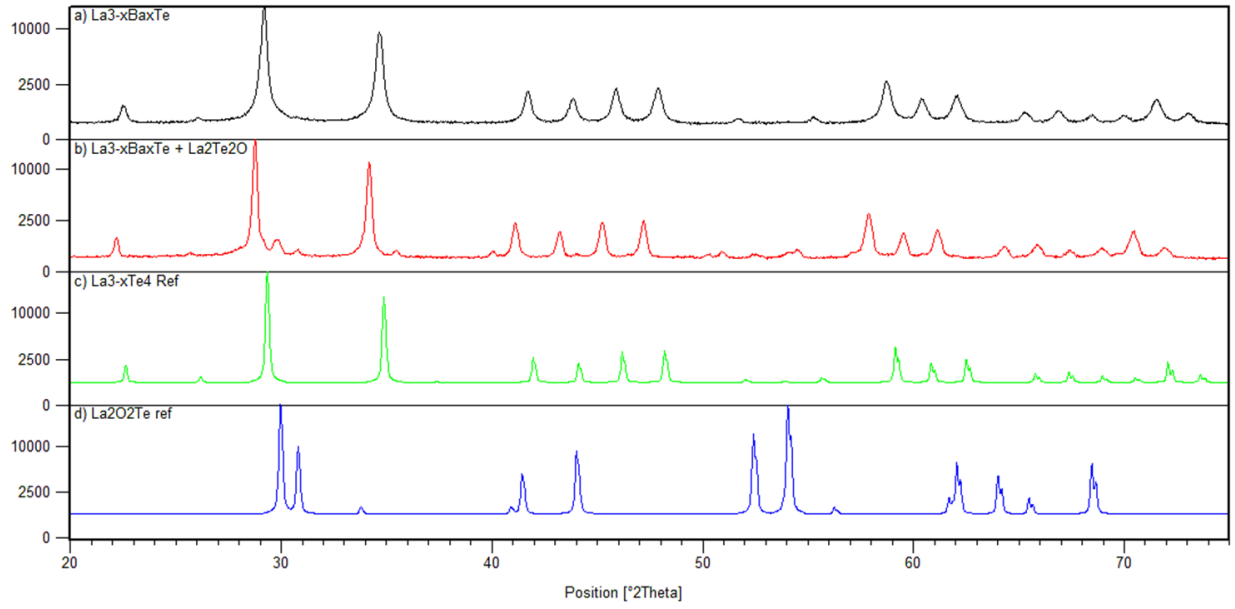

Figure 6.1 X-ray diffraction spectra of a) $La_{3-x}Ba_xTe$ exhibiting peak shifts to lower angles reflecting the larger size of the Ba^{2+} atoms; b) $La_{3-x}Ba_xTe_4$ which is contaminated by most likely La_2O_2Te; c) reference $La_{3-x}Te_4$ spectra JCPDF 01-073-1470; and d) reference La_2O_2Te spectra JCPDF 01-074-1267.

6.4 Evaluation of the Mechanical Properties of $La_{3-x}Te_4$-Ni Composites

The initial motivation for the development of $La_{3-x}Te_4$-Ni composites is to improve fracture toughness and strength. Initial work has indicated that the inclusion of Ni particles results in an improved fracture toughness, little change in hardness of the material, and allowed for the material to be tested to higher indentation loads (1 kgf) without spalling as seen in Fig. 6.2.

Examination of the fractured surface suggests that this is achieved through the crack bridging toughening mode (Fig 6.3) which is similar to what is observed in other ceramic-metal

composites[8]. Testing needs to continue to examine the effects of additional higher loading fractions on the hardness and fracture toughness.

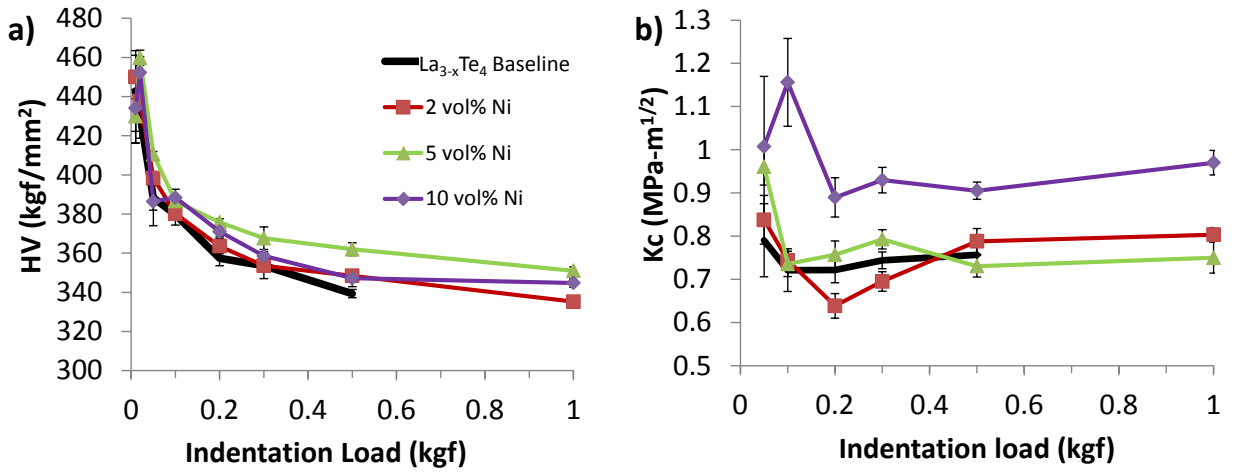

Figure 6.2 a) Vickers hardness of $La_{3-x}Te_4$ and $La_{3-x}Te_4$-Ni composites. b) Vickers indentation fracture toughness of $La_{3-x}Te_4$ and $La_{3-x}Te_4$-Ni composites.

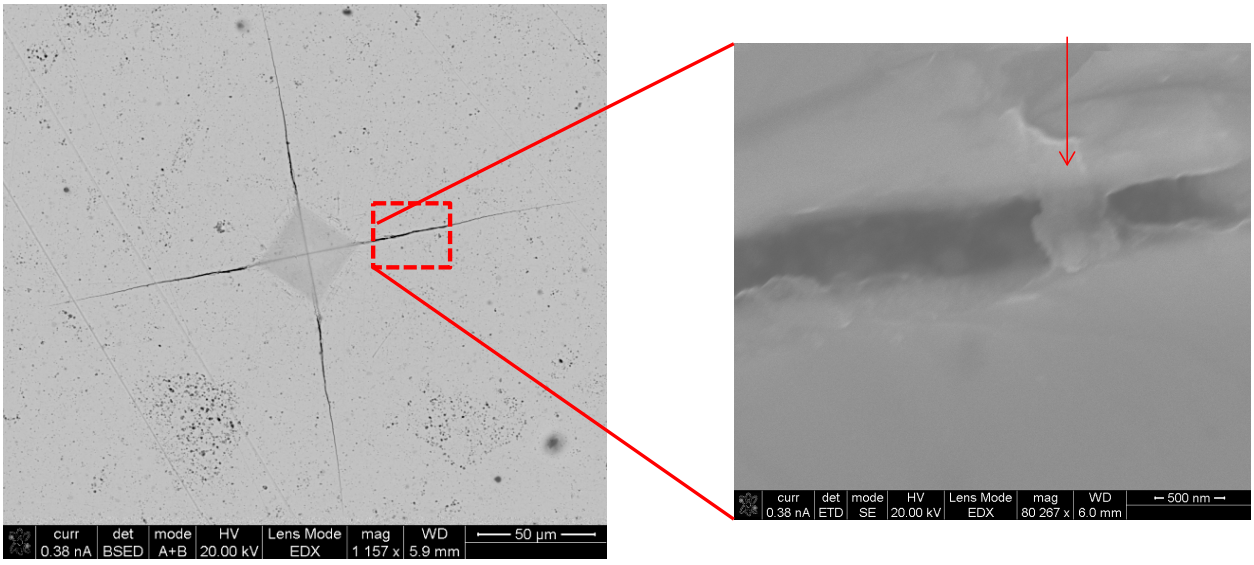

Figure 6.3 Scanning electron micrograph of $La_{3-x}Te_4$-Ni after a Vickers indent. The magnified micrograph shows what is likely a Ni ligament bridging the two faces of a crack leading to the observed enhanced fracture toughness.

In addition, initial results indicate that the inclusion of Ni particles improves the Weibull modulus and flexural strength of the $La_{3-x}Te_4$ as shown in Fig. 6.4. Additional samples need to be tested to examine the effect of higher loading fractions of Ni on the flexural strength. This testing could be achieved with N = 10 samples at loading fractions of 2, 5, 10, 15 vol%. The study will require an appreciable investment in time and resources, but will be a straightforward process and could lead to promising insights into improving the mechanical behavior of this material.

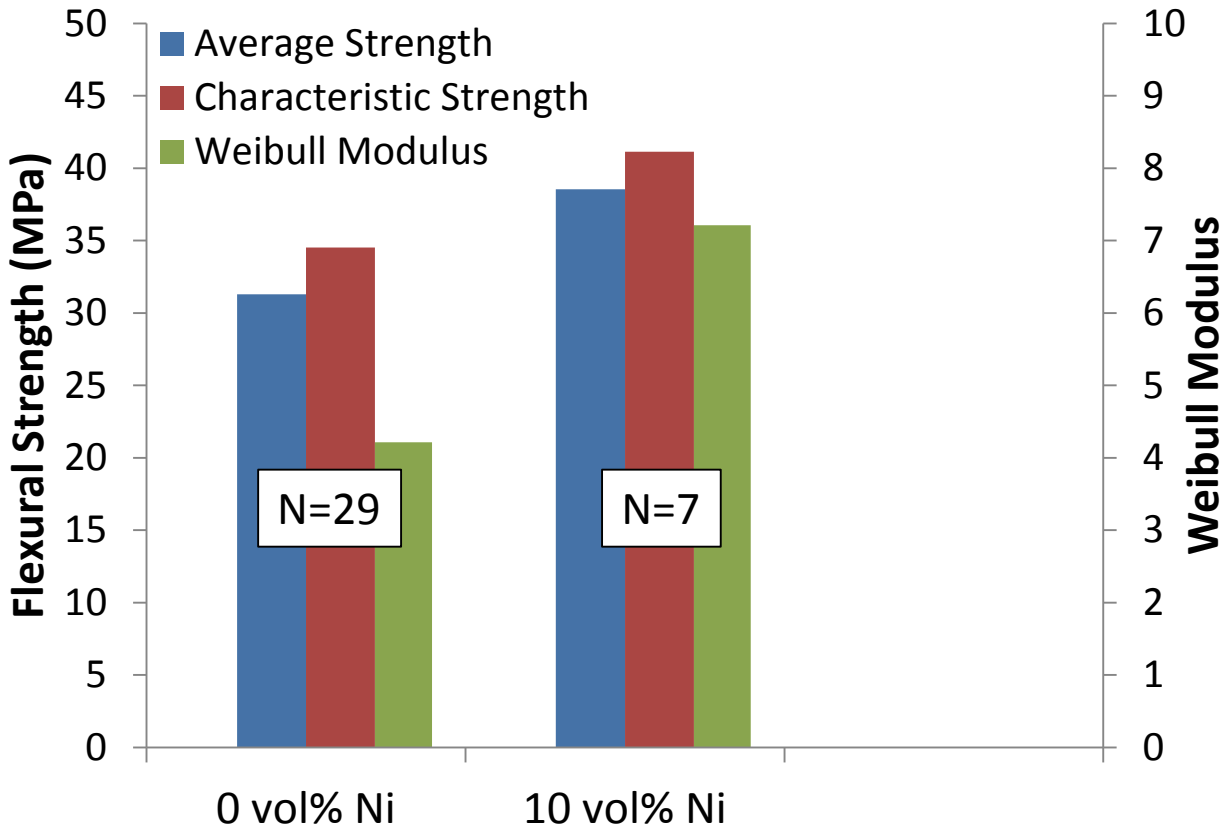

Figure 6.4 The flexural strength, characteristic strength, and Weibull modulus of a $La_{3-x}Te_4$ and a set of 10 vol% $La_{3-x}Te_4$-Ni composites. Initial results show improved flexural strength and higher reliability.

References

1. C. B. Vining, in *CRC Handbook of Thermoelectrics*, ed. D. M. Rowe, 1995, vol. 2.

2. R. D. Abelson, in *CRC Handbook on Thermoelectrics*, ed. D. M. Rowe, CRC Press, 2006.

3. D. R. Brown, T. Day, T. Caillat, and G. J. Snyder, *J. Electron. Mater.*, 2013, **42**, 2014–2019.

4. S. Bux, J.-P. Fleurial, T. Caillat, B. Y. Li, K. Star, S. Firdosy, V. Ravi, C.-K. Huang, B. Cheng, P. Gogna, J. M. Ma, P. von Allmen, and T. Vo, in *11th International Energy Conversion Engineering Conference*, American Institute of Aeronautics and Astronautics, 2013.

5. P. Ball and T. Caillat, *MRS Bull.*, 2013, **38**, 446–447.

6. A. F. May, J.-P. Fleurial, and G. J. Snyder, *Chem. Mater.*, 2010, **22**, 2995–2999.

7. O. Delaire, A. F. May, M. A. Mcguire, W. D. Porter, M. S. Lucas, M. B. Stone, D. L. Abernathy, V. A. Ravi, S. A. Firdosy, and G. J. Snyder, *Phys. Rev. B*, 2009, **80**, 1–9.

8. A. G. Evans, *J. Am. Ceram. Soc.*, 1990, **73**, 187–206.